Thesis for the degree of Doctor of Philosophy

Visualising Functional Nanostructures of Organic Semiconductors using Electron Microscopy

Gustav Persson

Department of Physics

Chalmers University of Technology

Gothenburg, Sweden 2024

Visualising Functional Nanostructures of Organic Semiconductors using Electron Microscopy

Gustav Persson

ISBN 978-91-8103-001-3
Doktorsavhandlingar vid Chalmers Tekniska Högskola
Ny serie nr 5459
ISSN 0346-718X

Department of Physics
Chalmers University of Technology
SE-412 96 Gothenburg
Sweden
Telephone +46 (0)31 772 3334

Cover image:

Upper left: HAADF-STEM image of the nanostructure of a p[p($g_4$2T-T)-co-U] copolymer thin-film.
Upper: EDXS spectral images of the interface in a bilayer p($g_4$2T-T):BBL film.
Upper right: BF-TEM image of the BHJ morphology of a TQ1:$PC_{71}BM$ sample, and implementation to a KMC model.
Center: JEOL NeoARM 200F TEM.
Lower left: 3D tomographic reconstructions of 5 mol% and 60 mol% Mo(tfd-$COCF_3)_3$ dopant clusters in p($g_3$2T-T) with markers for individual dopant molecules.
Lower: Conductivity plots of p($g_3$2T-T), p($g_4$2T-T) and p($g_6$2T-T) doped with 5-60 mol% Mo(tfd-$COCF_3)_3$.
Lower right: 3D tomographic reconstructions of 5 mol% and 60 mol% Mo(tfd-$COCF_3)_3$ dopant clusters in p($g_6$2T-T) with markers for individual dopant molecules.

Printed at Chalmers Reproservice
Gothenburg, Sweden 2024

Visualising Functional Nanostructures of Organic Semiconductors using Electron Microscopy

Gustav Persson
Department of Physics
Chalmers University of Technology

Abstract

Organic semiconducting materials have enabled the solution-processable fabrication of light-weight and flexible electronic devices. In particular, doping using molecular dopants has enabled the fabrication of high-performance organic electronics. Despite the significant progress in the last decades, organic electronics are still outperformed by their inorganic counterparts regarding device efficiencies, and an optimisation of the material properties is necessary. The properties of organic semiconductors have been shown to be correlated to their fine-scale microstructure.

In this thesis work, the nanostructure of organic semiconducting thin-films and the spatial distribution of molecular dopants are studied using electron microscopy. The aggregation characteristics, the morphology of the phases and the detailed interface structure have been studied using transmission electron microscopy. The films have been studied using two- and three-dimensional imaging and spectroscopy. The results show that the electrical properties depend on the nanostructure. Furthermore, the three-dimensional spatial distribution of individual molecular dopants in the organic semiconductors is revealed by electron tomography. The dopants are present as individual species or in clusters. The cluster size increases as the dopant concentration increases. The polar side-chain length for a semiconducting polymer is shown to affect the cluster size, where short side-chains lead to a more fine-dispersed distribution. This promotes the charge transfer from the dopants to the surrounding polymer, resulting in increased ionisation efficiency and increased electrical conductivity. The nanostructure-conductivity correlation provides important information for the understanding of the fundamental mechanisms determining the electrical conductivity in the doped organic semiconductors, which in turn enables the optimisation of the properties.

Keywords: organic semiconductor; nanostructure; molecular dopant; concentration; clustering; structure-property correlation; transmission electron microscopy; visualisation; 3D

List of appended papers

This thesis is based on the following papers:

Paper I
Toughening of a Soft Polar Polythiophene through Copolymerization with Hard Urethane Segments
Sepideh Zokaei, Renee Kroon, Johannes Gladisch, Bryan D. Paulsen, Wonil Sohn, Anna I. Hofmann, Gustav Persson, Arne Stamm, Per-Olof Syrén, Eva Olsson, Jonathan Rivnay, Eleni Stavrinidou, Anja Lund and Christian Müller
Adv. Sci., 2021, 8, 2002778

Paper II
Ground-state electron transfer in all-polymer donor–acceptor heterojunctions
Kai Xu, Hengda Sun, Tero-Petri Ruoko, Gang Wang, Renee Kroon, Nagesh B. Kolhe, Yuttapoom Puttisong, Xianjie Liu, Daniele Fazzi, Koki Shibata, Chi-Yuan Yang, Ning Sun, Gustav Persson, Andrew B. Yankovich, Eva Olsson, Hiroyuki Yoshida, Weimin M. Chen, Mats Fahlman, Martijn Kemerink, Samson A. Jenekhe, Christian Müller, Magnus Berggren and Simone Fabiano
Nat. Mater., 2020, 19, 738–744

Paper III
Experimentally Calibrated Kinetic Monte Carlo Model Reproduces Organic Solar Cell Current–Voltage Curve
Sebastian Wilken, Tanvi Upreti, Armantas Melianas, Staffan Dahlström, Gustav Persson, Eva Olsson, Ronald Österbacka and Martijn Kemerink
Sol. RRL , 2020, 2000029

Paper IV
Visualisation of individual dopants in a conjugated polymer: sub-nanometre 3D spatial distribution and correlation with electrical properties
Gustav Persson, Emmy Järsvall, Magnus Röding, Renee Kroon, Yadong Zhang, Stephen Barlow, Seth R. Marder, Christian Müller and Eva Olsson
Nanoscale , 2022, 14, 15404-15413

Paper V
Impact of Oligoether Side-chain Length on the Dopant Distribution and the Electrical Properties of Polar Polythiophenes
Gustav Persson, Sri Harish Kumar Paleti, Magnus Röding, Sophie Griggs, Junfu Tian, Jesika Asatryan, Yadong Zhang, Stephen Barlow, Seth R. Marder, Jaime Martin, Iain McCulloch, Christian Müller and Eva Olsson
In manuscript

My contributions to the appended papers

Paper I: I prepared samples for TEM analysis together with my co-authors. I performed the TEM experiments, interpreted the results together with my co-authors and wrote parts of the manuscript together with my co-authors.

Paper II: I prepared FIB-SEM cross-sections of the sample for TEM analysis. I performed the TEM imaging and spectroscopy experiments together with my co-authors, interpreted the results together with my co-authors and wrote parts of the manuscript together with my co-authors.

Paper III: I performed the TEM experiments, interpreted the results together with my co-authors and wrote parts of the manuscript together with my co-authors.

Paper IV: I planned the study and I prepared TEM samples together with my co-authors. All TEM experiments, tomography reconstructions and dopant identification using markers were performed by me. I was involved in the data analysis using MATLAB script together with my co-authors. I interpreted all results together with my co-authors. I wrote the first draft, I wrote the manuscript and the revision of the manuscript together with my co-authors.

Paper V: I presented and initiated the concept of the study. The details were planned together with my co-authors. I prepared samples for TEM analysis together with my co-authors. All electron microscopy experiments, including SEM imaging, TEM imaging, tilt series acquisition and tomography reconstructions were performed by me. I evaluated the tomography reconstructions with my co-authors. I was involved in the quantitative evaluation of the tomography data together with my co-authors. I interpreted all results with my co-authors. I wrote the first draft and wrote the manuscript together with my co-authors.

Acknowledgements

The research presented in this thesis was carried out in Eva Olsson Group, Division of Nano- and Biophysics in the Department of Physics, Chalmers University of Technology, Gothenburg, Sweden, during the period of December 2018 to March 2024. The work was performed under the supervision of Prof. Eva Olsson and co-supervisor Prof. Christian Müller.

The thesis work was funded by Swedish Research Council grant 2016-06146, and this support is gratefully acknowledged.

The time spent with this project has been life-changing, and I would like to offer my sincerest gratitude to the following persons who have joined me along the way: My main supervisor Eva for all your guidance and support during the ups and downs of this thesis work, for showing me the world of electron microscopy and for creating an incredibly inspiring working environment. My co-supervisor Christian for introducing me to many concepts in the field of organic electronics and the fruitful discussions during the Organic Electronics Journal Club meetings. All the members of Eva Olsson Group; you are a fantastic group that I can always rely on for difficult scientific questions and for simple cheerful conversations. The more than 7 years I have been a part of the group have really flown by, and I have enjoyed every moment with you. Special thanks go to Jonatan for being an excellent officemate and a great company. I would also like to thank Sri, Emmy and Sepideh from Müller group and Magnus from RISE; none of this would have been possible without your collaborations and insightful suggestions. Many thanks to Stefan and Ludvig from Chalmers Material Analysis Laboratory for the training and the perpetual support with the microscopes, and to Ola for all the technical support. A big thank you to all the love and support I have received from my mother, my father and my sister, from my partner Elin, and from my dog Bob. And finally I would like to express my gratitude to you, for taking your time and reading this thesis.

Declaration of Transparency

This thesis is a continuation of the work published in the licentiate thesis "Correlating Nanostructure and Electronic Properties of Organic Semiconductors by Electron Microscopy" by G. Persson, Chalmers University of Technology, 2022. [1] All chapters have been updated and expanded upon based on the final results of the thesis project.

List of Abbreviations

2D two-dimensional

3D three-dimensional

4T quaterthiophene

BBL poly(benzimidazobenzophenanthroline)

BHJ bulk heterojunction

F_4TCNQ 2,3,5,6-tetrafluoro-7,7,8,8-tetracyanoquinodimethane

HOMO highest occupied molecular orbital

LUMO lowest unoccupied molecular orbital

Mo(tfd)$_3$ molybdenum tris(1,2-bis(trifluoromethyl)ethane-1,2-dithiolene)

Mo(tfd-CO_2Me)$_3$ Mo(tfd)$_3$ with -CO_2Me side-groups

Mo(tfd-$COCF_3$)$_3$ Mo(tfd)$_3$ with -$COCF_3$ side-groups

P3HT poly(3-hexylthiophene-2,5-diyl)

PA polyacetylene

PBTTT-C_{14} poly[2,5-bis(3-tetradecylthiophen-2-yl)thieno[3,2-*b*]thiophene]

PC_{71}BM (6,6)-phenyl-C71-butyric acid methyl ester

p(g_x2T-T) thiophene based polymer with oligoethylene glycol side-chains

P(NDI2OD-T2) poly{[N,N'-bis(2-octyldodecyl)-naphthalene-1,4,5,8-bis(dicarboximide)-2,6-diyl]-*alt*-5,5'-(2,2'-bithiophene)}

p(p($g_4$2T-T)-co-U) copolymer with p($g_4$2T-T) and urethane units

TQ1 poly[2,3-bis-(3-octyloxyphenyl)quinoxaline-5,8-diyl-alt-thiophene-2,5-diyl]

OFET organic field-effect transistor

OLED organic light-emitting diode

OPV organic photovoltaic

OSC organic semiconductors

OTE organic thermoelectric

PCE power conversion efficiency

TEG thermoelectric generator

ADF annular dark-field

BF bright-field

BSE backscattered electron

DF dark-field

EDXS energy dispersive X-ray spectroscopy

EELS electron energy-loss spectroscopy

FIB-SEM focused ion-beam scanning electron microscope

FTIR fourier-transfer infrared spectroscopy

GIS gas injection system

GIWAXS grazing-incidence wide angle x-ray scattering

HAADF high-angle annular dark-field

KMC kinetic monte carlo

NMR nuclear magnetic resonance

SE secondary electron

SEM scanning electron microscopy

SI spectral imaging

SIRT simultaneous iterative reconstruction technique

STEM scanning transmission electron microscopy

TEM transmission electron microscopy

UV-Vis-NIR ultraviolet-visible-near infrared

WBP weighted back-projection

Contents

1 Introduction

1.1 Background

Since the development of the transistor, electronic devices have become an integral part of modern society. Electronics has now evolved into a key industry, with significant research and development being devoted to improving transistors in computers, light-emitting diodes for lighting, solar cells for energy production and many other devices. [2] The majority of modern electronic devices are based on silicon, a semiconducting element that is abundant in the earth's crust but requires energy-intensive and polluting extraction and refinement in order to be used for high-quality electronics. [3] An interesting alternative to silicon is electronic devices based on organic semiconductors. Electronic devices made of organic semiconductors are associated with light weight, mechanical flexibility, high tuneability and biocompatibility. The device fabrication is also theoretically less energy-intensive compared to its inorganic counterparts, making it interesting for more environmentally friendly technology and for sustainable energy production from devices such as organic solar cells and organic thermoelectrics. However, current organic electronics are generally outperformed by their inorganic counterparts regarding long-term stability and device efficiency. [4–6] Despite significant progress in the last decades, there are still uncertainties regarding fundamental mechanisms in the materials. Understanding and controlling such mechanisms can help improve the performance of organic electronics. [7, 8]

In recent years, significant research has been dedicated to exploring how the material micro- and nanostructure are connected to relevant device properties. [8–12] Examples of such analyses are phase separation in polymer blends and dopant distribution in doped organic semiconductors. [13–16] Electron microscopy is an excellent technique for the study of the material's functional nanostructure, with the potential to resolve details even at the atomic length-scales. [17,18] At this high spatial resolution, electron microscopy also enables analytical techniques to map out chemical distributions and variations in electronic structure. [19] But analysis with electron microscopy brings challenges of its own. Organic semiconductors are generally sensitive to damage from the electron beam in the microscope, and care

needs to be taken to not destroy the sample before relevant information can be collected. [20] This beam sensitivity has historically limited the studies of the material, but modern advancements in instruments and strategies have reduced this problem and increased the applicability of electron microscopy as a technique for high spatial analysis of organic semiconductors. [13] The versatility of advanced electron microscopy techniques are now well-suited for study of structure-property relationships in organic electronics.

1.2 Scope of the thesis

The focus of this thesis is to contribute to a better understanding of the functional nanostructures in organic semiconductors. Aggregation characteristics, phase morphology and the detailed structure of the interfaces in organic semiconductor systems are of importance. The nanoscale distribution of dopant species in organic semiconductors is another crucial aspect addressed in this thesis. The nanostructure is visualised using advanced electron microscopy techniques. Subsequently, the experimentally obtained information is analysed and correlated to electrical properties relevant for device applications.

This thesis is structured in the following way:
Chapter 2 provides relevant background information regarding organic semiconductors and organic electronic devices.
Chapter 3 describes the investigated materials, the experimental methods used for characterisation and how samples were prepared for analysis.
Chapter 4 shows the results from the studies and discusses their implications.
Chapter 5 finally summarises the conclusions from the study and provides an outlook for future work.

2 Organic Semiconductors (OSCs)

The term 'organic electronics' describes electronic devices made from carbon-based semiconducting materials, so called organic semiconductors (OSCs). [21] These materials offer great potential, but also big challenges to implement in practice. This thesis is focused on the analysis of OSCs and its implications when used as the active material in organic electronics. Therefore, this chapter provides background information regarding OSC theory. The first section introduces the fundamentals of OSC materials and molecular doping. The second section discusses the nanostructure of OSCs and its relationship to material properties. The final section presents device applications and the crucial aspects of OSCs in organic photovoltaics and organic thermoelectrics.

2.1 Fundamental Concepts for OSCs

This section introduces some fundamental concepts for organic semiconducting materials. General material properties are explained, how they can be changed through processing and why they are interesting for use in electronic devices are all discussed in the section. Molecular dopants are also introduced, which are crucial for the practical application of OSCs in electronics. Finally, the complex charge transport mechanisms in OSCs are described.

2.1.1 Intrinsic OSCs

OSCs are a class of carbon-based compounds with semiconducting, electrochemical and optical properties that are of interest for use in a broad range of electronic applications. The two main types of OSCs are conjugated polymers and organic molecular semiconductors such as fullerene derivatives. [21, 22] They are a promising alternative to inorganic semiconductors due to relatively low-cost materials with the possibility of efficient roll-to-roll processing. They can be applied in light-weight and flexible devices, and the tuneability of these materials allows optimisation of electronic and physical properties. OSCs have been known since

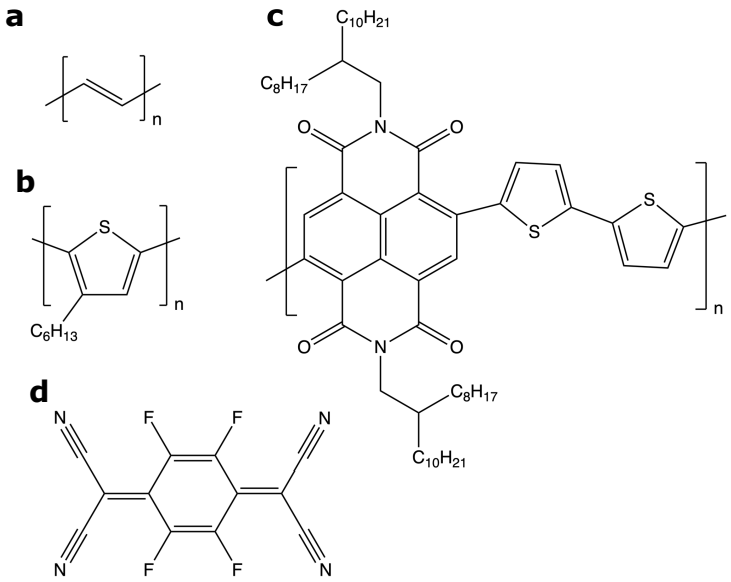

Figure 2.1: Examples of how the complexity of OSC molecular structures has increased over the years. (a) Polyacetylene (PA), (b) Regio-regular poly(3-hexylthiophene-2,5-diyl) (P3HT) and (c) Poly{[N,N'-bis(2-octyldodecyl)-naphthalene-1,4,5,8-bis(dicarboximide)-2,6-diyl]-*alt*-5,5'-(2,2'-bithiophene)} (P(NDI2OD-T2)). (d) Dopants' complexity have also increased, from alkali metals and halide atoms to molecules like 2,3,5,6-tetrafluoro-7,7,8,8-tetracyanoquinodimethane (F_4TCNQ).

1834, but only experienced isolated studies until the 1970's. [22] The work of MacDiarmid, Heeger and Shirakawa on polyacetylene, which resulted in the Nobel price in chemistry year 2000, [23] inspired further studies in the field and multiple critical discoveries in the following years. The initial efforts mainly focused on OSC conductivity, but as the materials progressed into functioning devices there was also a shift towards a better fundamental understanding of structure-property relationships and interest in new application-relevant metrics such as long-term stability. [22] As multiple properties have been taken into consideration, the molecular structures of OSCs used in electronic devices have grown in complexity. The research on improving structure and electronic properties have lead to relatively complex OSC molecular structures that are optimised for use in organic electronic devices. [24] Examples of the increasingly complex molecular structures of relevant OSCs are shown in figure 2.1. Among these examples, P3HT (figure 2.1b) will be mentioned multiple times in this thesis. With its relatively simple chemical structure, consisting of a polythiophene backbone and an apolar alkyl side-chain, it is commonly used as a model polymer. [25–27]

Electrically, OSCs behave like semiconductors. This means that similarly to their inorganic counterparts, there is a notable separation in energy between the highest occupied molecular orbital (HOMO) and the lowest unoccupied molecular orbital (LUMO). The difference in energy between HOMO and LUMO is termed the band gap. By tuning the band gap to an appropriate level the material may either act as an insulator, or as a conductor if sufficient energy is applied externally for the electrons to overcome the band gap. It is the possibility of manipulating semiconductors to control the electron motion that has made semiconducting materials a fundamental part of electronic devices. The semiconducting properties in organic materials come from sp^2-hybridisation of bonds between carbon atoms, meaning that carbon forms spatially confined bonds (σ-bonds) and delocalised bonds (π-bonds) with neighbouring atoms. The π-bond is not as energetically deep as the σ-bond, and is responsible for the optoelectronic properties of the material. When an electron overcomes the band gap and is promoted to one of the unoccupied energy levels, it also frees the state in the energy level it left behind, creating a positively charged quasi-particle called a hole. [21] Materials can be designed to preferentially transport either electrons or holes, where electron transporters are often referred to as n-type materials and hole transporters as p-type materials. These names do not refer to the ability to transport charges but rather how easily charges can be injected from electrodes that are used in devices, which in turn is associated with energy levels of the material. If the electron affinity of the material is closely matched to the electrode Fermi level, it is n-type. If the ionisation energy is close to the Fermi level, it is p-type. Efficient charge transport requires that charges move through the material without becoming trapped or scattered. [28]

The values of the energy levels vary for different semiconductor materials. These values can also be fine-tuned. A pure semiconductor is known as an intrinsic semiconductor, and these are seldom used if a high electrical conductivity is desired. Instead, the material properties of the semiconductor can be adjusted through a process known as doping, which will be explained in the following section.

2.1.2 Molecular Doping

Pure semiconductors are seldom used in state-of-the art electronic devices. By introducing a small amount of impurities into the material the Fermi level can be shifted and electron or hole conductivity can be increased manyfold. This process is known as doping, and is well-established in the field of inorganic semiconductors in order to enhance device efficiency. [8] Typically, a low concentration of atoms (ratios in the range of $10^{-6} - 10^{-3}$) is covalently bonded with the host atoms to either add electrons in donor states (n-type doping) or holes in acceptor states

(p-type doping). [29] In the example of crystalline silicon, small amounts of boron atoms can be introduced for p-doping or phosphorous atoms for n-doping, generating mobile charges without disrupting the crystalline structure. The charge transfer efficiency of this process tends to be high for inorganic semiconductors, typically generating one free charge carrier per dopant atom, which as a result leads to a dramatic increase in conductivity even at these low concentrations. [30] Since doping allows for a high control over electrical parameters in inorganic semiconductors, organic semiconductors need a similar process in order for their devices to work at a similar level.

Interestingly, the first organic electronic applications almost exclusively used intrinsic semiconductors, not utilising the potential benefits of doping. The reason for this was that the first attempts of doping organic semiconductors used alkali metals and halides as dopant atoms, which does not covalently bond with the organic molecules and therefore have a tendency to diffuse around in the material. [31] Doped layers therefore became unstable under operating conditions. A solution to this problem is to use larger organic molecules as p- or n-dopants. [30] Controlling the molecule's size or shape has allowed a better control of diffusion and enhanced stability of doped layers. [8] Molecular doping has been a huge success for practical applications, allowing energy level alignment in modern devices and conductivity enhancement by several orders of magnitudes. Despite the success, introducing these organic molecules has also added new complexity to organic semiconducting systems, and fundamental mechanisms are still under debate. The doping efficiency in molecularly doped organic semiconductors are much lower than in inorganic systems. To counterbalance the low efficiency, a larger fraction of dopants is used for practical applications. The concentration of dopants in OSC systems is commonly in the range of multiple mole percent. These large concentrations have in turn shown to have a significant impact on the material structure, turning crystalline areas to amorphous and increasing the density of traps and scattering centres for charge carriers upon doping. Structural changes upon doping are usually not desired, and significant effort has been put into achieving higher dopant ionisation efficiencies at lower dopant concentrations. Depending on the choice of molecular dopant or semiconducting host, free charges can be generated through a number of different chemical mechanisms, but neutral dopants are understood to have two general types of interaction mechanisms: ion-pair formation (full charge transfer) or charge complex formation (partial charge transfer). [30]

In the case of ion-pair formation the dopant is completely ionised, *i.e.* a p-dopant will extract an electron from the host OSC and a n-dopant will donate an electron

to the host, leading to a localised charge on the dopant and an opposite charge in the OSC matrix. Experimental observations from a number of systems have pointed towards the validity of this ion-pair formation model, but there have also been exceptions. [32] This has been explained through the model of charge transfer complexes, or partial charge transfer. A charge transfer complex may form as a hybridisation of overlapping molecular orbitals for dopant molecule and host OSC. This will form new, local HOMO and LUMO levels notably different from the original HOMO and LUMO of the OSC and the dopant, where the new degree of hybridisation and energetic splitting is dependent on the initial energetic and spatial overlap. The charge will be shared between dopant and OSC in the charge complex, so this case leads to a partial charge transfer as opposed to a full charge transfer in the case of ion-pair formation. As a consequence, the charge transfer complexes must be thermally activated in order to create free charges, which leads to generally lower doping efficiencies and conductivities compared to ion-pair formations. [8, 33]

The ionisation efficiency of dopant molecules has also been shown to be affected by disorder in the OSC system. As dopants are added and contribute with charges to the OSC, the resulting dopant ions remain in the system and generate local electrostatic fields that can be felt by other molecules. This will introduce an electrostatic disorder. With a random distribution of dopant molecules, the resulting fields will randomly shift energy levels of local molecules and give rise to an energetic disorder. The energetic disorder can be determined from the broadening of the system's density of states as a result from the disorder. A correlation between energetic disorder and structural disorder is theoretically predicted for OSC systems. As an example, recent studies have used simulations to show that even fine-scale clustering of a few dopant molecules can lead to a significant widening of the density of states. This widening indicates an increase in energetic disorder, which in turn has a negative impact on electrical conductivity. [34] Other simulations have shown that device-relevant parameters such as dopant ionisation efficiency can be affected as a result of the increased disorder after doping. [35] The impact of dopant nanoscale distribution will be further discussed in section 2.2.2.

2.1.3 Charge Transport in Doped OSCs

The electrical conductivity in OSCs is commonly described using the classical formula for semiconductors:

$$\sigma = q\mu n \tag{2.1}$$

for the electrical conductivity σ, the elementary charge q, the charge mobility μ and the charge density n. [36] However, fundamental understanding of charge transport, and how to effectively control these parameters, has proven to not be straightforward. The soft nature of OSCs, which is advantageous from a processing and application viewpoint, results in more complex charge transport compared to inorganic semiconductors. Inorganic semiconductors commonly have strong covalent bonds between atoms, enabling them to be grown as highly ordered crystals. This results in an electron wavefunction which is typically delocalised over the crystalline lattice. However, due to their molecular nature, this is not the case for OSCs. The π-conjugated electronic states tend to be delocalised within a molecular unit, but intermolecular bonds are often of weak nature such as van der Waals forces. This results in a soft and less ordered solid, with electron wavefunctions delocalised over only a small number of molecules. The ability to delocalise over multiple molecular units is dependent on molecular structure and intermolecular packing in an OSC. [21, 37] Spatial disorder, the size and weight of molecules, molecular packing and the presence of impurities are factors that can affect the charge mobility in OSCs. [28] Additionally, since each molecule perceives a different surrounding, the HOMO and LUMO levels in the material will vary around an average value, giving rise to an energetic disorder. A consequence of this disorder is generally lower charge mobility. Thus, it is important to consider processes over multiple length-scales in order to understand all factors of charge transport in these materials. [21, 37]

The intermolecular charge mobility is usually lower compared to the intramolecular mobility in OSCs. Due to the disorder, adjacent molecules will be separated by a potential barrier that needs to be overcome for transport between them. Overcoming this barrier therefore becomes a tunnelling process, dependent on spatial separation and energy differences between the adjacent states. At temperatures above 0 K, fluctuations in thermal energy may allow a jump between molecules. This jumping manner of charge transport common for OSCs is termed hopping, and this is generally the rate-limiting step which determines conductivity. Hopping has been found to be a suitable charge transport model for a large fraction of conjugated polymers. It should be noted, however, that transport characteristics can differ due to chemical or morphological variations between OSCs. As an example, some polymers may contain ordered high-mobility domains embedded within low-mobility disordered domains. If chains that connect the high-mobility domains are present, they can form conductive pathways which significantly increases the overall charge transport. [21] The importance of nanoscale morphology in OSCs is further discussed in section 2.2.

Additionally, the charges transported through OSCs are typically not electrons or holes. It is common for organic molecules to have an equilibrium geometry that is different in ionised state compared to its ground state. Specifically, after doping an organic polymer chain, it can be energetically favourable to spatially localise the transferred charge on the chain and have a local distortion around the charge. If the relaxation energy gained from this distortion is greater than the energy required to have a distorted lattice, the charge becomes spatially bound with a binding energy equal to the energy difference. This formation is called a polaron, and is a charge-matter coupling where a charge becomes spatially bound to the place of distortion in the host. [31, 38] A schematic of the material energy levels before- and after polaron formation are shown in figure 2.2. In order for hopping transport to occur for a polaron, an activation energy related to its binding energy needs to be overcome. [39] The localised nature of polarons has a negative impact on overall conductivity, and it is important to consider polaron delocalisation in order to reduce this effect. The exact delocalisation of polarons depends on the system, but as an example recent modelling suggests that polarons are delocalised over 10-20 molecules (or monomers) for some high-performance OSCs, *i.e.* over a few nanometers. [40] As new dopants are added, it can also be energetically favourable to add a second charge adjacent to the polaron rather than somewhere else along the polymer chain, forming a new electronic species instead of two lone polarons. The new specie will form if the lattice interaction is greater than the Coulomb repulsion between the two charges confined to the same location. [38] This new doubly-charged specie is either referred to as a bipolaron, if the polarons are spin-paired, or as a polaron pair, if the single polarons are strongly coupled but without any spin-pairing. Adding polarons, bipolarons or polaron pairs causes new localised electronic states around the OSC band gap due to local shifts of HOMO and LUMO, making new electronic transitions available. The formation of bipolarons instead of polarons is generally not desired, since bipolarons are associated with a lower mobility and thus lower conductivity. A recent study also suggests that the dopants' position relative to the OSC is crucial for stabilising bipolarons. [41]

Despite its complex nature, the progress in understanding charge mobility has allowed the fabrication of OSCs with higher mobilities than that of amorphous silicon. However, there are still uncertainties regarding fundamental charge transport mechanisms, and a further understanding of these processes is crucial for the future development of organic electronic devices. [37]

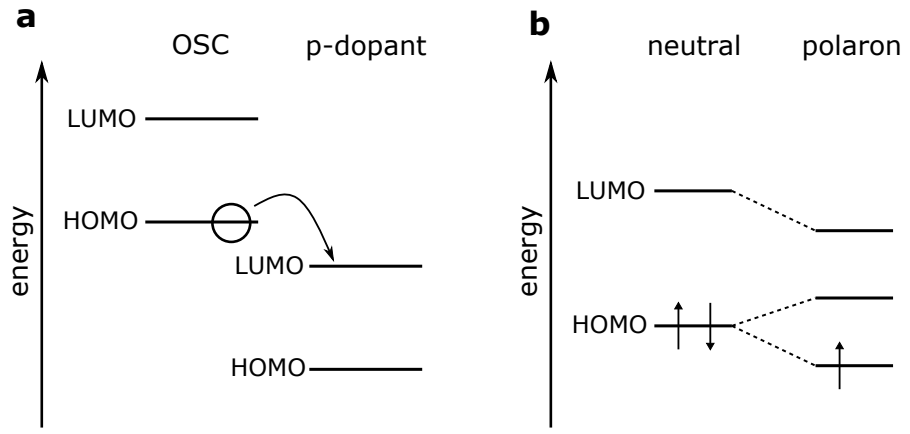

Figure 2.2: Energy levels in doped OSC systems. (a) Energies of an intrinsic OSC and a p-dopant. (b) Formation of a positive polaron after p-doping. The polymer reorganisation causes a splitting of the HOMO level into two sub-levels, resulting in new possible electronic transitions.

2.2 Nanostructure of OSCs

Due to the relationship between structure and properties in OSC, it is crucial to characterise the nanostructure of both intrinsic and doped OSCs in order to understand and control fundamental properties. This section explains how different nanoscale features in OSC systems affect their performance in applications. In particular, the relationships between distribution of molecular dopants, electrical properties and the OSC nanostructure are discussed in detail. The final part of this section describes how this relationship can be controlled by modifying the polymer side-chains.

2.2.1 Structure-Property Relationships in OSCs

It was understood at an early stage that transport properties in OSC materials are highly dependent on their nanostructures. In these heterogeneous structures, order can exist at length-scales ranging from atomic to microscopic and mesoscopic levels. One particular challenge that this heterogeneity presents is the understanding of how the spatial arrangement of these differently structured regions affects charge transport internally and across multiple regions. Due to this, characterisation techniques that analyse structure over multiple length-scales or a combination of different techniques are important for a greater understanding of structure-property relations within OSCs. [42]

As an example, understanding of how polymer chain alignment and the degree of crystallinity is connected to their mechanical properties have allowed the development of fibres with higher specific strengths than steel. [43] It was initially thought that a more crystalline microstructure would lead to a better transport than in disordered systems. This may often be the case for inorganic semiconductors, but this idea is challenged by observations of disordered or even amorphous polymers performing on par with semicrystalline polymers. It has been suggested that since charges have a short scattering mean free path in stacked molecules with a strong π-orbital overlap, they are mostly affected by short-range order in the material. Hence, charge transport would mostly be affected by short-range ordering and their interconnection in the material, and crystallites of multiple scattering lengths would bring very little additional benefit for the transport. Such short-range order is typically of the length-scale single nanometres. Based on this, it has been suggested that developing organic molecules with improved packing, orbital shape, symmetry and orientation can lead to enhanced transport properties in OSCs. [43, 44] Due to its dependence on molecular packing, OSCs can also display asymmetrical electrical properties along different orientations. Such anisotropy can even be manipulated by forcing the polymer chains along a certain direction. Tensile drawing and high-temperature rubbing are examples of techniques that can be performed to align the polymers, resulting in a significantly anisotropic charge transport. [45, 46]

Another structural aspect that is relevant for high charge mobility is the degree of π-stacking between conjugated polymers. As mentioned in section 2.1.1, the semiconducting properties of conjugated polymers come from delocalised π-orbitals along the chain. When packing multiple chains, it is possible to stack the polymer backbones cofacially such that π-orbitals of different chains will overlap. This stacking resulting in π-orbital overlap, or simply "π-stacking", leads to enhanced charge mobility due to a more efficient charge transfer between chains. [47] The degree of π-stacking in OSCs is commonly determined using X-ray diffraction techniques such as grazing-incidence wide-angle X-ray scattering (GIWAXS). GIWAXS has become a staple technique for analysing ordering in OSCs (although a recent study have shown that it can fail to identify ordered regions for some some high-mobility polymers). [48] The patterns obtained from GIWAXS can be further analysed using the Scherrer equation in order to calculate the coherence length L, which corresponds to the average size of π-stacked regions in the material. [49] A higher value for L means larger regions of ordered, π-stacked, regions in the material. Another popular metric for quantifying the OSC order is the paracrystalline distortion parameter g. g can also be calculated from GIWAXS data, and corresponds to the lattice disorder in paracrystalline regions. Thus, a lower value

is desired for a more ordered structure. [50]

2.2.2 Dopant Distribution in OSCs

The effectiveness of molecular doping has been closely linked to the structure of both dopant and host OSC. Incorporating dopant molecules changes the OSC nanostructural ordering, and the close connection between structure and electrical properties makes it important to analyse and understand these changes. Experimental observations imply that dopant molecules are not randomly distributed in the host OSC, but rather towards preferential sites. Blends of the polymer poly[2,5-bis(3-tetradecylthiophen-2-yl)thieno[3,2-*b*]thiophene] (PBTTT-C_{14}) and the molecular dopant F_4TCNQ show that F_4TCNQ has a tendency to intercalate between the conjugated backbones of the polymer, forming π-stacked aggregates and crystallites. A similar phase has been observed for F_4TCNQ-doping of quaterthiophene, 4T, where experimental data suggests that the dopant molecules incorporates into ordered polymer regions, forming crystalline dopant-polymer complexes with high density of dopants. The formation of such domains means that less ordered areas suffer from a deficiency of dopants and may limit the overall conductivity. [32, 51]

Studies of electronic properties as a function of dopant ratio often display a saturation of important parameters such as electrical conductivity past a certain point. Doping beyond this saturation point does not increase the system's conductivity, and for many cases it even leads to a decrease. The reasons for this are still not fully understood, and although suggestions have been made there is still too much unknown to accurately predict the how the dopants will affect conductivity in different OSC systems. [8] It has been suggested that morphology plays a crucial role in the flattening and eventual decline of conductivity at high doping concentrations. As dopant molecules becomes embedded in the host OSC, they form a new phase which may disrupt the system microstructure, leading to a reduction in charge mobility. [52] Larger aggregates of dopants have also been observed in doped systems, resulting in morphological changes that can be correlated with a saturation in conductivity. These aggregates can grow larger at higher doping ratios, up to a few hundred nanometers in size. As aggregates grow larger, a less efficient doping of the OSC can be observed. [53] In other systems, dopant aggregates have been reported to stop growing at certain sizes (*e.g.* around 20 nm), but the aggregates instead become more frequent in the film at higher doping concentrations. Interestingly, nuclear magnetic resonance (NMR) analysis on the same samples have shown a lack of unreacted dopants in these samples, indicating that the aggregates may contain a finer nanostructure that allows the dopants to re-

main in contact with the OSC. [54] The three-dimensional structure of aggregates can also be of high importance for the transport properties in the OSC. Donhauser *et al.* have shown that dopants may not only aggregate, but they can also form filamentous structures of dopants that connects one side of the thin film with the other. The formation of such filaments is expected to lead to highly anisotropic conductivity, with preferential charge transport at the film surface or within the vertically aligned nanostructures. [55] Such findings indicate that the nanostructure can be closely connected to electronic properties, and a better control over morphology is highly relevant for the fabrication of efficient OSCs.

Different doping schemes have been developed in attempts to better control the dopant-host OSC interaction. A common doping method is the "mixed-solution method", where the OSC is dissolved in a solvant and the dopant is added to the solution. The mixture of OSC and dopant is then used to directly form the film. An alternative to this is the "sequential doping method", where the undoped OSC is allowed to first form a film and then the dopant is dissolved in an orthogonal solvent and added to the already dried OSC film. Although the mixed-solution method allows better control of the final ratio between OSC and dopant and a higher maximum achievable doping concentration, sequential doping has the advantage that the OSC microstructure is formed in advance, and may be less affected by the dopant molecules. A comparison between mixed-solution and sequential doping of F_4TCNQ on P3HT have shown that surface roughness of mixed-solution films is significantly higher than for the same doping concentrations achieved through sequential doping. The authors conclude that the higher surface roughness comes from aggregation that happens in the mixed solution before the film microstructure has formed. In the same study it is also noted that the conductivity for sequentially doped films is higher than for films doped through mixed-solution at the same dopant concentration. [56] Another way to perform sequential doping is through vapour deposition, where an undoped OSC is first formed and then exposed to dopant molecules in vapour phase which sublimes in the film. Doping through vapour deposition has also proven to be effective at preserving the OSC nanostructure. [57]

After electron transfer between dopant and host OSC, the dopant molecule will remain in the system as a counter-ion. The dopant counter-ions do not covalently bond, but commonly bind with weak forces such as van der Waals or Coulombic interactions. These weak binding forces can relatively easily be overcome, resulting in changes in the dopants' spatial locations through diffusion or drift. It has been shown that the diffusion process requires an activation energy close to the thermal energy at room temperature, meaning that extensive rearranging

of the dopants' spatial distribution can happen over time, which in turn may severely affect the long-term stability of organic electronic devices. Dopant diffusion in organic electronics was a major reason why atomic dopants were abandoned in favour of small molecules which are less mobile. Although this change seems to have improved long-term stability, diffusion is still a significant problem for applications. Studies on dopant diffusion have concluded that the rate of diffusion is dependent on dopant molecule size and shape and also the nanostructure of the host OSC. The F_4TCNQ molecule is relatively small and has a planar structure. Bulky, three-dimensional dopant molecules are expected to have lower diffusion rates, and may be promising for an increased long-term stability on the systems. [58] An example of a well studied bulky molecular dopant is molybdenum tris(1,2-bis(trifluoromethyl)ethane-1,2-dithiolene) ($Mo(tfd)_3$), an organometallic molecular dopant where three tfd units are arranged in a trigonal prismatic geometry around one Mo atom. It is a p-dopant with a high electron affinity, promising stability and in recent years a more solution-processable version, $Mo(tfd\text{-}COCF_3)_3$, has been synthesised by addition of ester groups. [59, 60] However, the three-dimensional structure also means that the molecule displaces more volume in a host OSC, which could lead to a higher degree of morphological disruption and lower maximum doping levels. [61]

Due to the larger size of $Mo(tfd)_3$-derivatives, the dopants are expected to not be able to enter the π-stacked crystallites of P3HT at room temperature. However, a study has reported a higher diffusion of $Mo(tfd\text{-}CO_2Me)_3$ in regioregular P3HT than regiorandom P3HT, despite that the more ordered regioregular P3HT should contain a higher fraction of crystalline regions. [62] The article suggests that the higher diffusion could be explained by a higher free volume in grain boundaries or connecting regions between crystallites in regioregular P3HT. This example shows how the nanostructure of these systems is often complex and interpretation may not be straightforward.

A heterogeneous dopant distribution within the OSC can lead to a Fermi level gradient over the material, which in turn will cause a static electric field. Despite that such an electric field might affect dopant diffusion properties or impose drift across layer interfaces, there are only a few studies regarding this matter. [8] One study that analysed the drift of $Mo(tfd\text{-}CO_2Me)_3$ in P3HT and a small molecule OSC noted that significant drift could be induced after applying an electrical field across the doped material. After placing a thin film between two electrodes and applying a moderate electrical field relevant for device applications, the authors demonstrated a drift of several micrometers. Such drift may lead to a significant inhomogeneity of electrical properties in the material due to depletion of dopants

in some regions and accumulation of dopants in others. Interestingly, the same study showed that the drift could be reversed by changing the direction of the applied field. Doping drift over several micrometers is detrimental for the efficiency of organic field-effect transistors, solar cells and organic light-emitting diodes, and although the effect may be less severe for some material systems it could still be of interest for understanding long-term device degradation. [63]

Molecular doping is crucial for the fabrication of high-performance OSCs, but nanostructure related problems such as aggregation have proven to limit their performance. A recent strategy to reduce the impact on the nanostructure is through double doping, *i.e.* dopants where the molecules may transfer two electrons each. This could result in that lower doping concentrations are needed for the devices. [64] Another strategy that is explored in this thesis is to avoid these problems through ground-state electron transfer. By engineering energy levels of the components in OSC blends, electron transfer may spontaneously occur at their interfaces which results in highly conductive pathways. This will be described in more detail in section 4.1.2.

2.2.3 OSC Side-chains and Nanostructure

It has been shown that engineering of polymer side-chains can help the dopant insertion mechanism in the polymer matrix. After demonstrating that F_4TCNQ dopants mainly locate in the layers of alkyl side-chains in P3AT and PBTTT-C_n, a systematic analysis of the effect of changing the alkyl side-chain length for the polymers shows that there exists an optimum chain length for hosting dopants, and longer or shorter side-chains lead to slower dopant kinetics and lower final doping levels. The studies conclude that the longer side-chains in PBTTT-C_{18} leads to a highly ordered and tightly packed structure, which decreases the dopants ability to diffuse efficiently into the film. On the other hand, for PBTTT-C_8 the side-chains are too short, leading to a disordered structure which also may prevent efficient intercalation. Hence the loosely packed side-chains of PBTTT-C_{12} seem to yield the highest F_4TCNQ doping level for PBTTT-C_n, and P3HT (*i.e.* C_6 side-chains) is determined to be optimal for polythiophenes with alkyl side-chains. [65, 66]

Changing from apolar alkyl side-chains to polar side-chains is another option that has been explored for doping of conjugated polymers. Kroon *et al.* compared F_4TCNQ-doping of P3HT and p($g_4$2T-T), where both polymers have a polythiophene backbone but the latter contains polar oligoethylene glycol side-chains. The study showed a higher maximum conductivity of doped p($g_4$2T-T) than for doped P3HT, and this was partially attributed to a better dispersion of dopants due to the

polar side-chains, which do not form crystalline dopant aggregates even at higher concentrations. The authors also noted a significantly higher thermal stability for doped p($g_4$2T-T), which was rationalised with a stronger interaction between the molecular dopants and the polar side-chains. [67] Since polar side-chains repel each other, the effect of changing the side-chain length is not necessarily the same as for apolar side-chains. The effect of varying polar side-chain length has been tested for derivatives of fullerene, which is an organic semiconducting small molecule, showing that it is possible to fine-tune doping efficiency and molecular ordering by optimising the side-chain length. [68] Thus, changing the polar side-chain length should also have an effect on the dopant distribution and electrical properties of conjugated polymers. A recent study has noted that the use of shorter polar side-chain has the potential to increase the electrical conductivity of doped polymers, which was attributed to a higher charge mobility in the material. [69] This topic is explored in paper V and discussed in section 4.2.3 in this thesis.

2.3 Organic Electronic Devices

After the initial work in the field of organic semiconductors in the 1980's, organic electronic devices began to emerge. Electrical conductivity was the common metric during initial years, but as development in the 1990's progressed into device application there was a pursuit towards new OSC architectures to optimise device efficiencies. Consequently, a better fundamental understanding of structure-property relationships was emerging. New metrics such as thermal- and light stability began to be of interest for specific applications. Devices that received significant attention were organic photovoltaics (OPVs), organic light-emitting diodes (OLEDs) and organic field-effect transistors (OFETs). [22] This thesis focuses on systems relevant for OPVs and another emerging technology called organic thermoelectrics (OTEs), and these devices are therefore explained in more detail in this section.

2.3.1 Organic Photovoltaics (OPVs)

Solar energy is suggested as one of the major forms of sustainable energy since sunlight equivalent to approximately 6000 times the global energy consumption reaches the earth's surface each year. This large theoretical potential has been a main argument for solar energy for a long time. The first solar cell based on silicon was invented 1953 [70], and already five years later the first solar module was used in space. Silicon has been established as the most common semiconducting material in industry for solar cells and multiple other electronic application areas. [70] But other types of materials have been investigated as candidates to replace silicon.

Organic photovoltaics can be seen as one of the more recent, emerging technologies. [71] In fact, on the global scale of energy production where the criterion of abundant raw materials becomes more relevant, only silicon- and carbon based photovoltaics are favoured. [72] Using OSCs as the active material in photovoltaics offers several advantages. High absorption coefficients means that only little material is needed and the material can be made into thin films. Thin films can be made on flexible substrates, resulting in light-weight, flexible photovoltaic panels. OPVs are also associated with simple fabrication methods that can be scaled up to industrial levels, and chemical synthesis allows many possibilities to tune mechanical, electrical and optical properties. [73] However, despite the positive aspects of OPV, the power conversion efficiency (PCE) and long-term stability of OPVs have historically been lower than their inorganic counterparts. The higher PCE and long-term stability of inorganic solar cells have led to a wider commercial spread of inorganic solar cells, but these devices suffer from relatively high energy costs and environmental issues. It has been suggested that tuning the device nanostructure can improve both the PCE and the long-term stability of OPV. [74, 75]

Converting sunlight into electrical energy involves several steps for OPVs, and each of these steps has to be optimised in order to avoid bottlenecks for the overall efficiency of the device. When a photon is absorbed by the active OSC layer, an electron is excited to the LUMO level and a hole is generated in the HOMO level. However, the excited electron and the resulting hole have a binding energy that keeps them together as an electron-hole pair, commonly referred to as an exciton, and this binding energy is significantly higher for OPVs compared to their inorganic counterparts. In order to overcome the exciton binding energy, OPV devices consisting of donor and acceptor OSCs have been developed, where the HOMO and LUMO energies are lower in the acceptor than those of the donor. From this follows that at the donor-acceptor interface, it is energetically favourable for electrons to transfer to the acceptor material and holes to the donor material, leading to splitting into charge carriers. An exciton has a finite lifetime before the electron-hole pair recombines and the photon energy is lost as lattice vibrations. In practice, excitons can diffuse a distance of typically 20 nm or less before recombination in OSCs. The active layer in OPVs should therefore minimise the distances between donor-acceptor interfaces in order to maximise the charge separation efficiency of excitons. [73]

An answer to this tough requirement is the bulk heterojunction (BHJ) structure, which has significantly improved the PCE of OPVs. In a BHJ, the donor and acceptor materials form a network with maximised interfacial area. An example

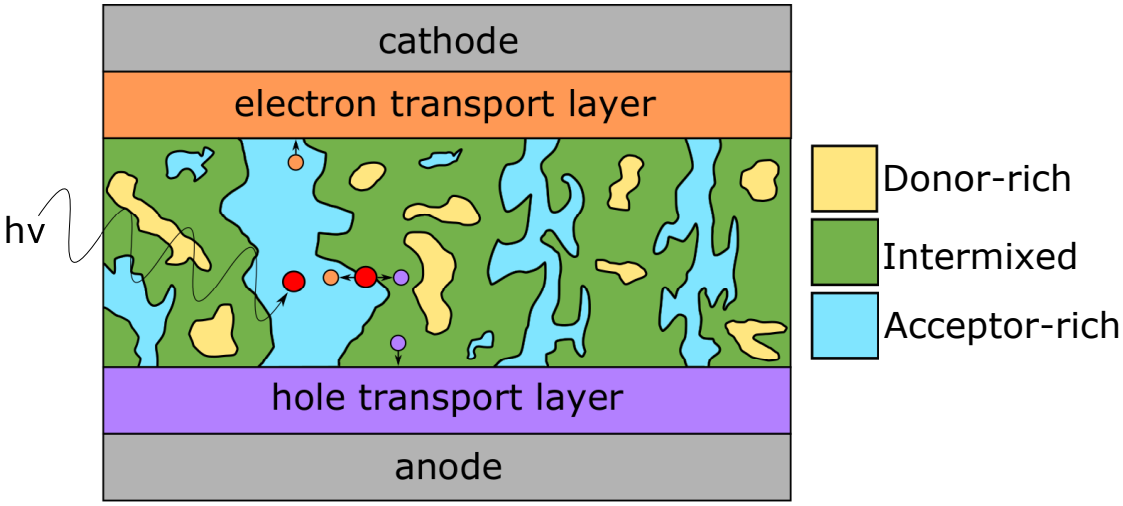

Figure 2.3: A typical architecture of an organic photovoltaic cell, with a bulk heterojunction (BHJ) active layer between transport layers and electrodes. The BHJ may contain donor-rich, acceptor-rich and intermixed phases. As photons are absorbed in an acceptor-rich or donor-rich phase, the generated excitons needs to diffuse to an interface in order to separate into charge carriers.

of such a structure is shown in figure 2.3. After exciton splitting, a BHJ needs to provide continuous pathways for the charges to be transported to the electrodes where they can be extracted. Similar to excitons, a charge may recombine before reaching the electrode, resulting in a loss to the overall OPV charge generation. [74] Recent studies have shown that efficient BHJs commonly consist of a combination of an intermixed phase, an acceptor-rich phase and a donor-rich phase. [76, 77] Additionally, the fraction of acceptor and donor in the phases may be tuned in order to optimise charge generation and charge transport. [78]

Fine-control of nanoscale distribution of the BHJ has proven difficult, and multiple studies have been published regarding the analysis and optimisation of commonly used OPV blends. [11,12,79] Even after achieving an optimal BHJ, the structure is often not thermodynamically stable and may degrade over time. Elevated temperatures have shown to speed up this process, and degradation of the fine-scale phase distribution of BHJ can be correlated to a decrease in device PCE. Exposure to air and even to some extent sunlight may also lead to degradation, reducing the OPV performance over time. Molecular engineering of OSCs that are resistant to these types of degradations is therefore seen as a method to increase stability. [75, 80]

The complete process of light harvesting in OPVs has been the target of intensive

research, which has led to an improved understanding and eventually the development of new record-breaking OSC blends. The OPV lifetime has now reached the time-scale of years [81], and the PCE of OPVs has reached more than 19 %. [82] However, high values of stability and efficiency are seldom realised simultaneously. Computer simulations have been suggested as a tool to better direct the molecular design of new OSC materials for OPVs, to predict properties and to hasten a more widespread commercialisation. Key properties such as electrical properties have proven difficult to model so far, but more recent models that include nanoscale structure have shown significant improvements in these aspects. [83] In paper III, the experimental data describing a BHJ nanostructure are used to improve the accuracy of electrical simulations, which will be further discussed in section 4.1.3.

2.3.2 Organic Thermoelectrics (OTEs)

Studies show that a large part of the energy produced globally is lost as waste heat. Efforts for a more sustainable energy consumption has drawn the attention towards thermoelectric generators (TEGs) that can directly convert heat to electrical energy. A thermoelectric generator is a device that utilises thermoelectric materials, *i.e.* materials that exhibit a strong Seebeck effect.

When a temperature gradient is applied over the material its dominant charge carriers will diffuse towards one side, effectively providing an electric potential. The strength of this thermoelectric effect can be described by a material parameter called the Seebeck coefficient, α. Doping can be used to control the dominant type of charge carriers in the material, *i.e.* holes or electrons. Electrons will diffuse towards the hot side in n-doped materials, while the holes will diffuse in p-doped materials. This control of charge carrier flow is used by a TEG, where two legs of different doping types are connected and put in a temperature gradient, giving rise to an electrical potential. Thermoelectric materials may also be used "reversely" by applying an electrical current to cool or heat an area. This ability to create a heat gradient from a difference in potential is called the Peltier effect. A schematic of the working principle of a TEG is shown in figure 2.4.

The quality of a thermoelectric material can be evaluated through a dimensionless thermoelectric figure of merit described by

$$ZT = \frac{\alpha^2 \sigma}{\kappa} T \tag{2.2}$$

where α is the Seebeck coefficient, σ is electrical conductivity, κ is thermal conductivity and T is the absolute temperature. As can be seen in equation 2.2, a dilemma

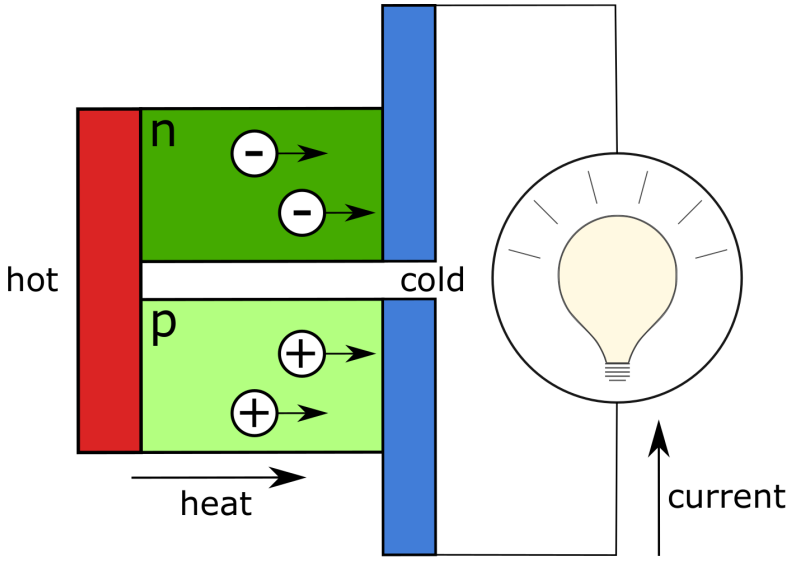

Figure 2.4: A simple schematic of a thermoelectric element consisting of two legs of oppositely doped thermoelectric materials. A temperature gradient over the materials results in an electric potential between the hot to the cold side. Connecting the p-type material with the n-type material gives rise to an electrical current.

of thermoelectric materials is that the maximum figure of merit is achieved by a high electrical conductivity and a low thermal conductivity. However, these material properties are usually linked, making the optimisation of thermoelectric materials difficult. [84, 85]

Despite this dilemma, there are multiple advantages of TEGs. Unlike most heat engines, the energy is directly converted without any intermediate conversion into mechanical energy that may involve losses. Since there are no moving parts in the device it is exceptionally reliable and usually boasts a long lifetime. TEGs can also be scaled from micro generation up to industrial applications. [86] Examples of areas where TEGs can be applied are waste heat recovery in vehicle exhaust gases and industry, power generation in remote areas and microgeneration for sensors and microelectronics.

However, low efficiencies and high cost have limited the spread of thermoelectric devices. In the last decades, inorganic semiconductors like Bi_2Te_3 and PbTe have been the main materials for thermoelectrics. While the materials have relatively reliable performance, they suffer from low abundance, high weight and toxicity. [86] However, the aspects where inorganic thermoelectrics suffer from

drawbacks are where thermoelectric devices made from organic semiconductors have the potential to excel. Organic thermoelectrics (OTEs) have started to be explored in more recent years. They have the advantage of being compatible with inexpensive and scalable fabrication methods, while being more lightweight, flexible and biocompatible compared to their inorganic counterparts. OTEs are also better at operating with smaller temperature gradients close to room temperature.

According to equation 2.2, a good thermoelectric material should have a high electrical conductivity and a low thermal conductivity. Inorganic thermoelectrics generally satisfy the first but not the second part, while the opposite is usually true for organic thermoelectric materials. The overall efficiency of OTEs are still lower than for their inorganic counterparts, and since κ is commonly satisfactory there has been considerable research focused on increasing the power factor $\alpha^2\sigma$. [87] Optimisation of the power factor has proven difficult, and studies have found that the Seebeck coefficient decreases as a function of conductivity according to the empirical relationship $\alpha \propto \sigma^{-1/4}$. In efforts to break this relationship, one aspect that has been studied in recent years is the conductivity's and Seebeck coefficient's dependence on the material structure. [88–90] One such study noted that a higher crystalline order in a doped polymer resulted in significantly improved electrical conductivity, but only small changes in Seebeck coefficient, leading to an increased power factor with increased structural order. [57] In another study, polymer chains were aligned by tensile strain which led to an anisotropy in the conductivity but kept the Seebeck coefficient relatively constant. [45] Similarly, polymer chain alignment using high-temperature rubbing has been observed to simultaneously increase both the electrical conductivity and the Seebeck coefficient. [91] These results show that alignment of polymer chains is a method to increase the thermopower along the strain direction and surpass the empirical relationship between α and σ. As mentioned in section 2.1.2, it has been recently noted that energetic disorder in the OSC may also affect device parameters such as the relationship between α vs σ in thermoelectrics. [34] Relations between structural disorder, energetic disorder and electronic parameters will be further discussed in section 4.3.

Flexible OSCs that can deform without fracture are highly relevant for OTE applications. [85, 92] This is possible for polymers that operate above their glass transition temperature T_g. Conductive polymers with polar side-chains has lower T_g than similar polymers with alkyl side-chains, resulting in mechanically "soft" materials with high flexibility to deform without fractures.[67] However, too soft materials may be problematic for the practical application of OTEs that require the mechanical robustness to form free-standing structures. [89] The fabrication of an OSC with both electrical and mechanical properties suitable for OTEs is de-

scribed in section 4.1.2, where the soft polymer p($g_4$2T-T) with polar side-chains is copolymerised with urethane segments in order to enhance mechanical stability.

Organic thermoelectric devices are complex systems, and the correlation between choice of OSC, dopant molecule, doping process and the resulting thermoelectric properties are not fully understood. [93] The development of OTE devices is still at an early stage compared to their inorganic equivalents, but their positive aspects continue to attract considerable research. Besides a focus on outperforming inorganic materials in classical thermoelectric applications such as power generation in remote areas, new areas may also be explored with the properties of OTEs. Flexible, lightweight modules that can perform with small temperature gradients open up applications in the future such as biointegrated and wearable devices, *e.g.* making use of the body heat to continuously provide power in artificial skin or in e-textiles. [87, 89] Great progress has already been made and although many challenges remain, continued research for a better understanding of the systems may lead to further success and an exciting future for OTEs.

3 Experimental

This chapter presents the materials and experimental methods chosen in this thesis for the study of functional nanostructures of OSCs. The studied materials are first introduced. This is followed by a thorough explanation of the main methods for structural characterisation. Finally, sample preparation as a prerequisite for these techniques is discussed in the last section.

3.1 Materials

As described in chapter 2, the properties of organic electronic systems may vary significantly depending on the choice of materials. This section introduces the OSCs and the dopant molecule studied in this thesis. The OSCs include the conjugated polymers p(g_x2T-T), poly(benzimidazobenzophenanthroline) (BBL) and poly[2,3-bis-(3-octyloxyphenyl)quinoxaline-5,8-diyl-alt-thiophene-2,5-diyl] (TQ1), and the organic small molecule (6,6)-phenyl-C71-butyric acid methyl ester ($PC_{71}BM$). The molecular dopant is Mo(tfd-$COCF_3$)$_3$. This text briefly discusses properties and reasons for interest in these OSCs and the dopant molecule. Finally, spin coating is discussed, which is a method to fabricate thin-film specimens from these materials.

3.1.1 p(g_x2T-T)

p(g_x2T-T) is a conjugated polymer that consists of a thiophene backbone, similar to well studied OSCs like P3HT, but with polar oligoethylene glycol side-chains instead of aliphatic to increase its processability in polar solvents. Three versions of p(g_x2T-T) with different side-chain lengths are studied in this thesis: x = 3, 4 and 6. The molecular structure of p(g_x2T-T) is shown in figure 3.1a. Figure 3.1b shows the molecular structure of the copolymer formed with urethane units, p[p($g_4$2T-T)-co-U], which will be further discussed in section 4.1.1.

A recent study has shown that doping p($g_4$2T-T) with the commonly used molecular dopant F_4TCNQ leads to electrical conductivities up to 100 S cm^{-1}. The

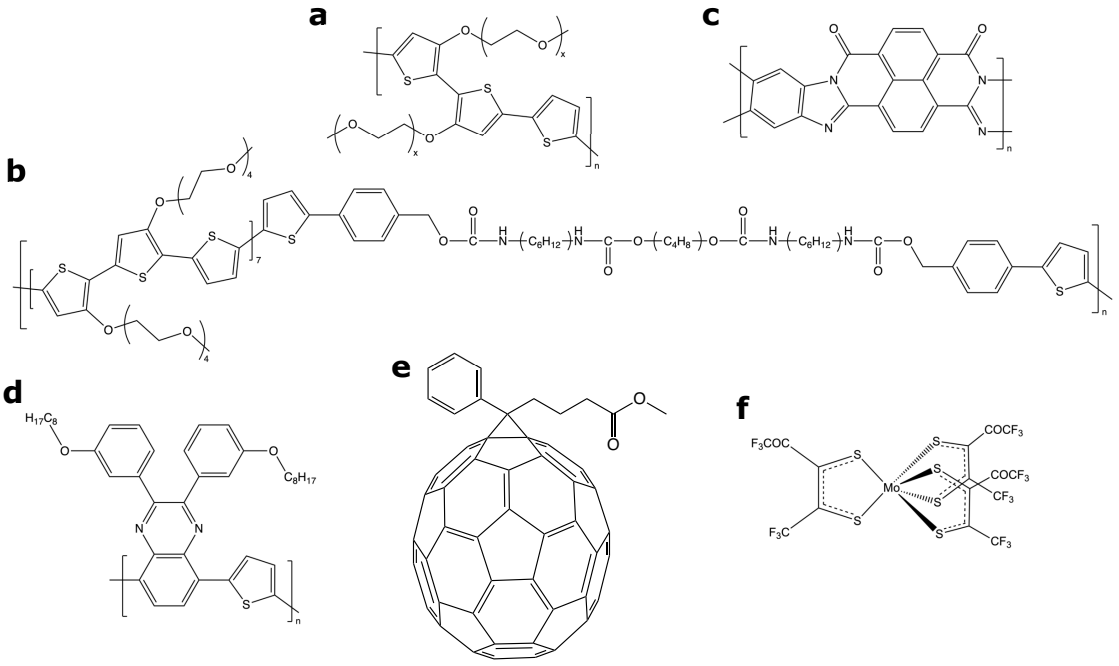

Figure 3.1: Molecular structures of the OSCs and molecular dopant used in this thesis work: (a) p(g_x2T-T), (b) p[p($g_4$2T-T)-co-U], (c) BBL, (d) TQ1, (e) $PC_{71}BM$ and (f) Mo(tfd-$COCF_3$)$_3$.

polymer's compatibility with these polar dopants also leads to a high thermal stability for the system, making it promising for use in applications such as OTEs. [67] Mixed-solution doping of OSCs such as P3HT with the dopant F_4TCNQ results in formation of ion-pairs which aggregate, leading to a suboptimal nanostructure. The study of p($g_4$2T-T) shows that adding polar side-chains is a promising design concept for suppressing this aggregate formation, reducing the losses in conductivity and thermal stability at room temperature coprocessing. [67] GIWAXS experiments in the same study show a lack of signal from F_4TCNQ crystals at higher dopant fractions, indicating that the dopant stays molecularly dispersed in the polymer even at higher concentrations. Although it has yet to be experimentally shown, the dopants are expected to be spatially located in the polymer side-chains, where the polar nature of the chains should improve their binding. It has also been speculated that a decreased density of side-chains, such as for p($g_4$2T-T) compared to P3HT, increases the available space for the dopant counter-ion which could lead to a higher degree of stability. [94]

3.1.2 BBL

BBL is a heteroaromatic polymer that has been well studied for its optical and electronic properties. Its molecular structure is illustrated in figure 3.1c. The BBL monomer has a two-dimensional geometry, resulting in a more limited conformational freedom and less hinderance for electron delocalisation for the polymer. Thus, BBL displays a high mobility for charge carriers. Doping has been used to form conductive BBL films that have shown high thermal stability [95], making it attractive for use in organic electronics such as OPV or organic field-effect transistors. [96] The high electron affinity and electron mobility makes BBL suitable for n-type transport layers in polymer-based devices. [97] Section 4.1.2 discusses a study of the interface structure of a p($g_4$2T-T):BBL bilayer.

3.1.3 TQ1:$PC_{71}BM$

BHJ blends of semiconducting polymers and small molecule fullerenes have been widely studied as donor and acceptor materials in OPVs. A fullerene derivate commonly used as acceptor material is $PC_{71}BM$. BHJ thin-films based on fullerenes tend to form high-performance active layers for OPV, which in part is due to a relatively stable nanostructure resistant to phase separation. The stable structure can be formed by heating $PC_{71}BM$ above its glass transition temperature (T_g), causing $PC_{71}BM$ to crystallise. This process is called thermal annealing. $PC_{71}BM$ have been shown to offer promising photovoltaic performance in blends together with the electron donor TQ1. TQ1 is an amorphous polymer that does not crystallise upon annealing. The difference in ordering and chemical composition between TQ1 and $PC_{71}BM$ have been used in previous studies to distinguish the two blend components. [98, 99] The molecular structure of TQ1 and $PC_{71}BM$ are displayed in figure 3.1d and 3.1e. The nanoscale phase distribution of a TQ1 and $PC_{71}BM$ BHJ have been investigated in this thesis, and the results from this study are discussed in section 4.1.3.

3.1.4 Mo(tfd-$COCF_3$)$_3$

In section 2.1.2, it is explained that many OSCs do not have a high electrical conductivity on its own and require doping using a molecular dopant to increase its applicability in organic electronics. High-performing molecular dopants often contain elements of similar atomic number as the host OSC, making it difficult to distinguish the dopant from its host when characterising the dopant spatial distribution. Such is the case for the commonly used F_4TCNQ. One molecular dopant with a distinct element is molybdenum tris-[1,2-bis(trifluoromethyl) ethane-1,2-

dithiolene], or $Mo(tfd)_3$. $Mo(tfd)_3$ is a p-type dopant, and besides being easier to identify during material characterisation since it contains the relatively heavy element Mo in a light-element surrounding, it also offers advantages to F_4TCNQ such as larger molecule size, higher electron affinity and a lower volatility. [59] In recent years, a more soluble derivative of $Mo(tfd)_3$ has also been synthesised by exchanging one -CF_3 side-group with -$COCF_3$ on each dithiolene ring. The resulting molecule, $Mo(tfd\text{-}COCF_3)_3$, is a relatively bulky molecular dopant shaped like a trigonal prism with a long axis approximately 1.2 nm in length and a short axis of approximately 0.6 nm. [60] It is expected that the three-dimensional shape of $Mo(tfd\text{-}COCF_3)_3$ would make it less prone to movement in the OSC compared to a dopant molecule with a planar structure such as F_4TCNQ. $Mo(tfd\text{-}COCF_3)_3$ is the molecular dopant used in the study described in sections 4.2 and 4.3, and its molecular structure is shown in figure 3.1f.

3.1.5 Thin-film Fabrication Using Spin Coating

OSCs are suitable to be made into thin-films for their practical applications. Since thin-films offer more mechanical flexibility than bulk materials, this form offers potential for devices that can bend and deform without permanent damage. [100,101] The absorption coefficient is generally higher for OSCs than for silicon, meaning that the majority of incoming sunlight can be absorbed in OPVs that use OSC thin-films as active layer. [70] Additionally, although vapour deposition and sequential doping offer a better potential to preserve the OSC nanostructure than doping through mixed solution, there is also risk for a dopant gradient forming in the film between the substrate side and the side that is exposed to the dopant vapour or solution, resulting in a heterogeneous distribution. [8] This gradient effect is reduced for specimens formed as thin films.

Spin coating is a well-established technique used to produce thin films with uniform thickness on flat substrates. This specimen fabrication technique is illustrated in figure 3.2. During spin coating, the solution of interest is dropped on a substrate which is accelerated up to a desired rotation speed. Common rotational speeds are in the order of thousands revolutions per minute, and at this rate the inertia of the solution causes it to flow radially. During this flow, the solution will cover the substrate and the solvent will evaporate quickly. Excess solution will be ejected from the substrate edges, leaving a thin film after the complete evaporation. The final thickness of the film depends on solution properties such as viscosity and volatility, and can be controlled through spinning parameters like rotation speed and total spinning time. [102]

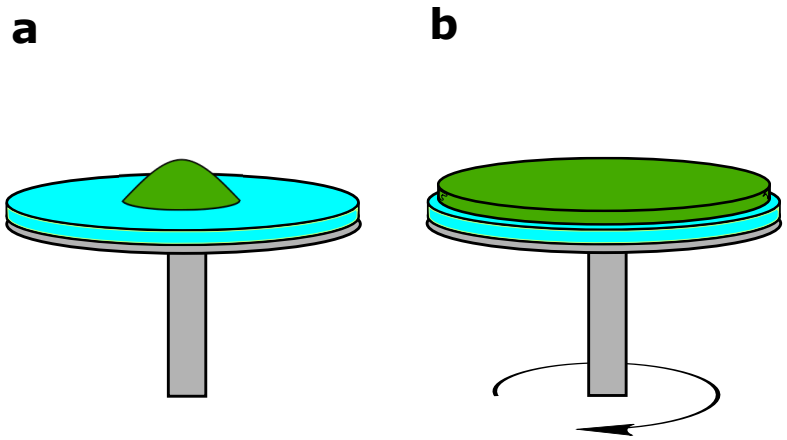

Figure 3.2: The main steps of the spin coating specimen fabrication technique. (a) A solution is dropped on a substrate. (b) Using high rotational speeds, the solution will flow radially and form a thin-film on the substrate.

3.2 Structural Characterisation

Since length-scales all the way down to nanometre or atomic levels are of importance for a thorough structural characterisation of organic electronics, techniques that can resolve such fine features are required. This thesis has focused on using electron microscopy for this detailed characterisation. In an electron microscope, electrons are accelerated by a high voltage and focused to an electron-dense beam using electromagnetic lenses. When this beam interacts with the investigated sample, multiple types of signals are generated that can be used for structural investigation at high spatial resolution. [19] Different forms of electron microscopes use this basic principle in different ways. This section explains the principles of the electron microscopy techniques used, and discusses the advantages and challenges of the different methods.

3.2.1 Scanning Electron Microscopy (SEM)

SEM was used in this thesis to screen for successfully fabricated samples, to gain an overview of the sample structures and for analysis at length-scales of 10-1000 nm. SEM is a flexible technique that allows characterisation of many different types of bulk samples. The main requirements are that the samples should not be electrically insulating or change structure when exposed to vacuum. A schematic of the basic SEM components is shown in figure 3.3. Electrons are emitted from an electron source, which is usually a thermionic gun or a field emission gun, and accelerated to high energies by an anode below the source. Energies used in

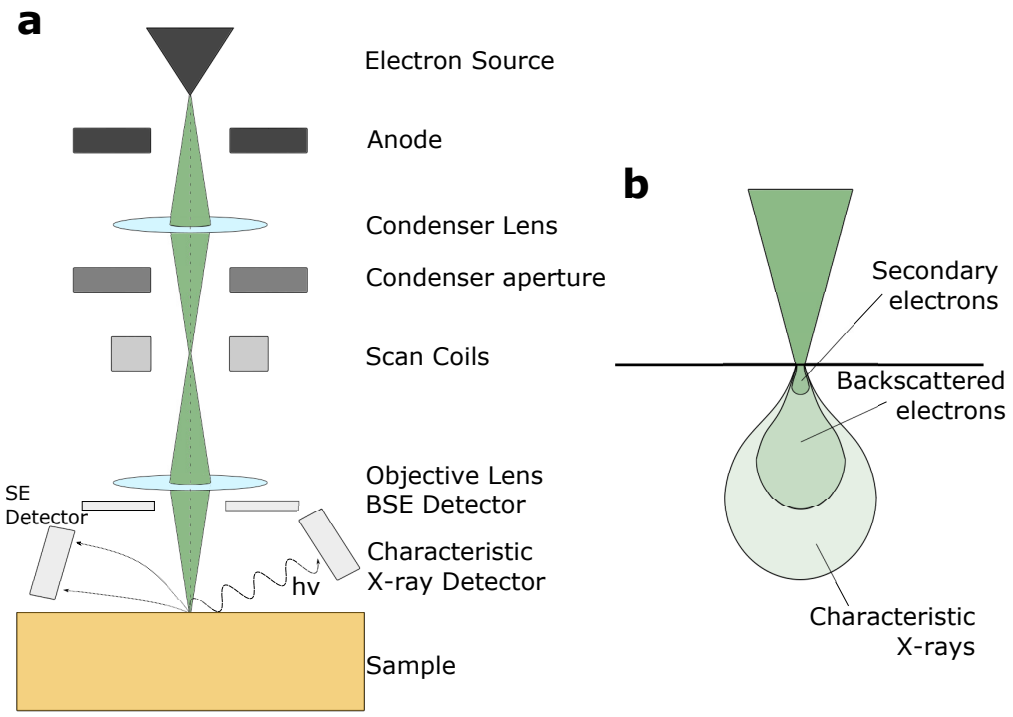

Figure 3.3: (a) A schematic of the basic SEM components and (b) three signal types that are generated when the focused electron beam interacts with the sample.

SEM typically range from 1 to 30 keV. Electromagnetic lenses in the microscope column are used to focus the electrons into a beam of high electron density. In SEM, the electron beam is further focused into a fine point, an electron probe, which converges at the sample surface. Using scan coils, the probe can then be raster scanned over the sample in order generate signals at different positions. These signals are collected pixel by pixel, and can be used to form an image of the analysed sample area.

Signals in SEM

As the electron probe interacts with the sample, elastic and inelastic scattering give rise to multiple types of signals that can be collected by detectors and used for structural and chemical analysis. The penetration depth of the electron beam in the sample is determined by the electron mean free path in the material. In general, a higher incident electron energy and a sample composed of lighter elements lead to a deeper penetration depth and a larger volume of interaction from

where signal can originate from. After formation, the signal also needs to escape the sample in order to reach a detector. The volumes from where different signal types can escape are not equal, leading to different effective interaction volumes. Three signals that are commonly used in SEM analysis are secondary electrons (SEs), backscattered electrons (BSEs) and characteristic X-rays. [103] Their interaction volumes are qualitatively shown in figure 3.3.

SEs are electrons originating from the sample. High-energy electrons from the beam may inelastically interact with electrons from the sample's atoms and eject them. These ejected sample electrons are the "secondary electrons", and have significantly lower kinetic energy than the electrons from the beam. Due to these low energies, SEs can relatively easily be reabsorbed by neighbouring sample atoms. Therefore, the interaction volume of SEs is small and localised to only the first atomic layers of the sample surface. The small interaction volume and reduced signal from deeper atomic layers make SEs useful for studies of a sample's surface topography in SEM. [103]

BSEs are electrons originating from the primary electron beam, and have higher energies than SEs. Incident electrons from the beam may elastically scatter against the sample atoms, leading to a large change in their trajectory. This is called backscattering. Since the energy of these scattered primary electrons is close to that of the incoming electron beam, backscattered electrons are not as easily reabsorbed by neighbouring sample atoms and their interaction volume is larger. The probability of backscattering is increased for heavier atoms, *i.e.* elements with higher atomic number Z, which therefore yield a higher BSE signal. The strong Z-number contrast makes BSEs useful for compositional studies in SEM. [103]

Characteristic X-rays are photons that are generated as the empty states, resulting from the secondary electrons escaping the atoms, are filled by electrons from outer electron shells. The relaxation will correspond to a specific energy difference that is unique for each electronic transition in each element, and will lead to the emission of a characteristic X-ray corresponding to the relaxation energy. The element specific energies of characteristic X-rays make them useful for elemental analysis in SEM. Since photons are massless particles they have a lower probability of reabsorption than electrons, and the resulting interaction volume is larger than for SEs and BSEs. [103] The spectroscopy technique of acquiring and analysing characteristic X-rays is further explained in section 3.2.4.

All SEM analyses in this thesis were performed on a JEOL JSM 7800F Prime equipped with a field-emission gun of the Schottky type as electron source and an

Oxford X-Max 80 mm^2 detector for energy dispersive X-ray spectroscopy (EDXS).

3.2.2 Transmission Electron Microscopy (TEM)

A transmission electron microscope (TEM) offers potentially higher spatial resolution than SEM, but it also adds the requirement of an electron transparent sample. Thus, this technique is not intended for bulk samples but is well-suited for detailed analysis of small sample volumes. The basic components of a TEM are illustrated in figure 3.4. Similar to SEM, electrons are first emitted from an electron source, accelerated to high energies by an anode and focused to a beam using electromagnetic lenses. TEM generally uses higher energies than SEM, with typical values ranging from 60 to 300 keV. In conventional TEM, a broad, parallell beam is used to illuminate the sample. In scanning TEM (STEM), the beam is instead focused into a small probe which converges at the sample and is raster scanned over an area, similar to SEM. Both of these modes were used for high-resolution analysis of the sample structures at the nanometre- and atomic levels. In TEM and STEM, the electrons are transmitted through the sample, producing signals through interactions with the sample atoms. The signals are used to extract high-resolution information of the analysed material. [19]

If high-resolution imaging using transmitted electrons is desired, the sample needs to be thin. Samples suitable for TEM analysis are commonly thinner than 100 nm, and materials consisting of elements with high Z-number may require even thinner samples. Additionally, using electrons that are transmitted through a sample means that an image formed from this signal is a two-dimensional (2D) projection of a three-dimensional (3D) material. Therefore, a reduced thickness also reduces the chances of multiple overlapping features in the depth direction, leading to more clearly interpretable images. [19]

Signals in TEM

Similarly to SEM, the interaction between the electron beam and the sample will produce SEs, BSEs and characteristic X-rays in a TEM. Despite this, the most commonly used signals come from the electrons that have transmitted through the sample. These signals can be divided into three main categories: Unscattered electrons, elastically scattered electrons and inelastically scattered electrons. Unscattered electrons are electrons that have transmitted through the sample without being scattered or scattered to small angles, and can be collected by a detector at the optical axis below the sample. Image formation using this signal is called

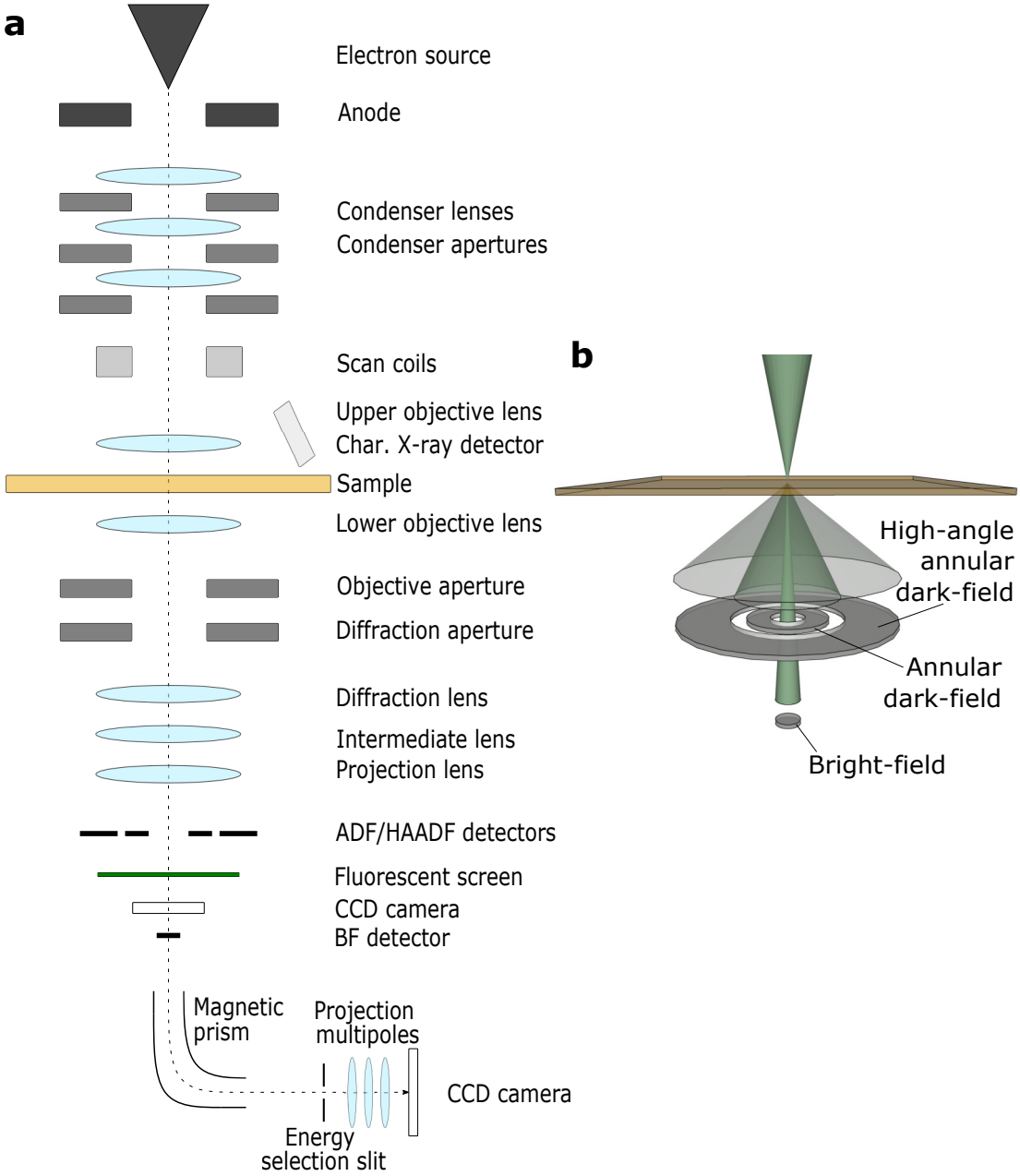

Figure 3.4: (a) A schematic of the basic TEM components and (b) three detectors that are used for collection of electrons scattered at different angle intervals when the focused electron beam interacts with the sample.

bright-field (BF) imaging, and is well-suited for phase-contrast imaging. In contrast to BF imaging, using the signal from electrons scattered at higher angles is instead called dark-field (DF) imaging. In this thesis, BF imaging has mainly been performed in TEM mode and DF imaging has been performed in STEM mode. Scattered electrons can be detected using an annular dark-field (ADF) detector, which is ring-shaped with a circular hole in the centre in order to exclude the unscattered electrons. ADF imaging using a sufficiently large hole, or more specifically with an inner acceptance angle larger than 50 mrad, is termed high-angle annular dark-field (HAADF) imaging. [19] The majority of the signal at these high angles is due to elastic electron scattering close to the nuclei of the sample atoms, making HAADF imaging more sensitive to variations in Z-number compared to BF- and ADF imaging. The practical Z-dependence of HAADF-STEM signal varies between $Z^{1.6}$ and $Z^{1.9}$, meaning that heavy elements will produce a strong contrast when surrounded by lighter elements. HAADF imaging is often termed Z-contrast imaging due to this dependency. Denser or thicker regions in a material means more mass to transmit through, which also leads to increased scattering and a higher HAADF signal. [104] Another advantage of using HAADF imaging is that coherent scattering is suppressed for electrons that are scattered to these high angles, which minimises the image contrast from Bragg scattering. Imaging crystalline samples at angles that fulfil Bragg's law gives rise to Bragg scattering, meaning that the contrast of certain regions may change at these angles and structures risk being misinterpreted in the images. [105] The suppression of Bragg scattering in HAADF images is important when performing electron tomography, which is discussed in section 3.2.3. Finally, inelastically scattered electrons are electrons that have scattered and deposited energy in the sample, and can be used as signal for a spectroscopy technique called electron energy-loss spectroscopy (EELS). As an electron is inelastically scattered, it may lose energy corresponding to the state it interacted with. Information such as elemental distribution and the chemical state of the element can be obtained using EELS in a TEM. [106]

The STEM analysis in this study was mainly performed using a FEI Titan 80-300 at an electron acceleration voltage of 300 kV. The instrument is equipped with a Schottky field-emission gun and a CEOS probe aberration corrector, allowing the STEM electron probe to be focused to a diameter of 70 pm. The microscope is additionally equipped with an Oxford X-sight EDXS detector for analysis of characteristic X-rays. HAADF-STEM was selected as the main imaging mode. BF-TEM in the study described in section 4.1.3 was performed using a FEI Tecnai T20 at 200 kV acceleration voltage equipped with a LaB_6 filament. HAADF-STEM imaging and analysis using characteristic X-rays in the study in section 4.1.2 was performed using a JEOL NeoARM 200F at 200 kV. This instru-

ment has a Schottky field-emission gun, an ASCOR probe aberration corrector and a CETCOR image aberration corrector and is equipped with dual EDXS detectors for analysis of characteristic X-rays.

3.2.3 Electron Tomography

Although it is possible to achieve high spatial resolution analysis using TEM, a limitation for structural analysis is that a transmitted signal will yield 2D projections of the sample and information regarding depth distribution of features will not be retained. This can complicate the interpretation of data and may even lead to wrong conclusions regarding the sample structure. A method developed to solve this problem is electron tomography. The base principle of tomography is to retain the 3D structure of an object by acquiring a series of 2D images at different tilt angles. By tilting the sample relative to the electron beam, the different images will contain information about the object from different viewpoints. Mathematical algorithms can then be used to reconstruct the full 3D volume from the acquired tilt series. [107] The algorithm used for reconstruction may vary, but the principle is based on the projection theorem (also known as the Fourier slice theorem). The theorem states that a projection of an object at a certain angle is equivalent to sampling of a central plane at the same angle in the object's 3D Fourier transform. This means that the series of projections in real space at different angles can be Fourier transformed, used to fill in the corresponding angles in its 3D Fourier transform, and finally inverted to reconstruct its 3D structure in real space. [108] A cartoon of how a 3D object is reconstructed from a 2D tilt series is shown in figure 3.5.

The resolution of tomographic reconstructions is not isotropic for the different axes, and will besides the microscope resolution also be limited by the number of images in the tilt series and its span of angles. With this in mind, one might reason that a tilt series over the full $\pm 90^{\circ}$ rotation over a sample with extremely fine rotation increments should lead to the best possible 3D resolution for the reconstructions. In practice however, the maximum tilt angles are limited by shadowing from the TEM sample holder, the grid or other features in the sample. The angles outside the maximum tilt lead to a missing wedge of information that can lead to an elongation and may introduce artefacts for the reconstructed features. [107] The missing wedge results in an elongation of the reconstructed structures, which is primarily along the reconstructed axis. However, this elongation can be calculated and corrected for. [109, 110] In practice, tilt steps of 1-2° with a tilt range of $\pm 70^{\circ}$ are commonly used for tomography experiments. These parameters should theoretically produce an elongation factor smaller than 1.3, which is usually deemed

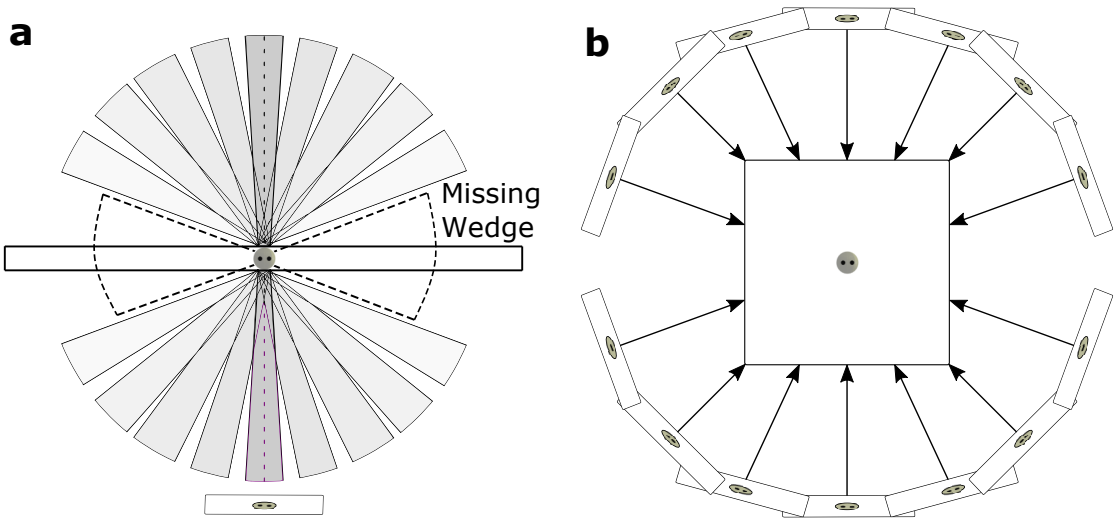

Figure 3.5: Cartoon illustrating the principle of electron tomography, where (a) a series of 2D projections of an object from different tilt angles is used to (b) reconstruct its 3D structure.

to be acceptable. Although the number of images in the tilt series does not have a theoretical maximum, exposing the same area of the sample for too high dose of the electron beam may damage the sample features and irreversibly change the structure during the acquisition. Sample damage from the electron beam is discussed in further detail in section 3.2.5. [111]

Direct reconstruction through inverse Fourier transform have shown to be computationally expensive and also requires a continuously varying function from series based on discrete sampling, which necessitates an interpolation that can affect the reconstruction results. Instead, the Radon transform has been widely used for tomography, which avoids the complications with inverse Fourier transform and the required interpolation. However, reconstructions using inverse Radon transform, commonly called back-projection, are known to produce 3D reconstructions with blurred fine details due to oversampling of information at low spatial frequencies and undersampling at high frequencies from the tilt series. This has been solved by convolving the reconstruction with a weighting filter that increases amplitude at higher frequencies, resulting in the popular weighted back-projection (WBP) reconstruction algorithm. A more modern approach is to iteratively reconstruct the volume, which is used in the algorithm simultaneous iterative reconstruction technique (SIRT). The main idea behind iterative algorithms is that the original TEM images can be seen as ideal 2D projections of the sample, but the missing information due to only a discrete number of samplings may lead to errors in the

final reconstruction. By iteratively comparing linear re-projections of the reconstruction with the original images, such artefacts can be removed from the output 3D structure to improve the results. [111]

A requirement for the reconstruction algorithms is that changes in image intensity should be linearly proportional to the change in sample thickness. This can make BF tilt series problematic to use for tomography on crystalline samples due to Bragg contrast at certain angles. However, this is not a problem for tilt series using HAADF imaging, which suppresses coherent scattering as described in section 3.2.2. Hence, HAADF-STEM images series are used for all tomography reconstructions in this thesis work.

3.2.4 Energy-Dispersive X-ray Spectroscopy (EDXS)

As described in section 3.2.1, when the primary electron beam causes inner shell electrons to be ejected from the sample atoms, electrons from outer shells will undergo relaxation to the vacant lower energy states. The energy difference of the two electronic states may give rise to a characteristic X-ray photon with a unique energy specific for each electronic transition in each element. This process is illustrated in figure 3.6. The spectroscopy technique of collection and analysis of these characteristic X-rays is known as energy-dispersive X-ray spectroscopy (EDXS), and has been widely used as a reliable technique for compositional analysis. In SEM and STEM, the raster scanning of the beam can be utilised to gather the X-ray signal pixel by pixel and correlate this to the beam position to combine the information of elemental composition with high spatial resolution. This process is known as spectral imaging using EDXS (EDXS-SI). As mentioned in section 3.2.1, characteristic X-rays are associated with a larger interaction volume in SEM, but the higher acceleration voltage and thin samples used in TEM significantly limit this signal spread and sub-nanometre resolution of the elemental distribution can be obtained. Modern software has made EDXS analysis streamlined and efficient, but it is important to know the underlying processes in order to acquire high-quality data.

In general, EDXS analysis of light elements can be more challenging than analysis of heavy elements, especially when the elemental concentration is low. This is due to that relaxation of outer-shell electrons will not always lead to emission of characteristic X-rays, instead Auger electrons may be emitted that are not detected by EDXS. The probability of characteristic X-ray emission increases with atomic number, and thus a higher signal per dose is achieved for heavier elements. [112] Furthermore, the characteristic X-rays are sent out in random directions from the

sample, and the limited space in the sample chamber allows only a fraction of the X-rays to reach the EDXS detector. After reaching the detector, X-rays are separated (or "dispersed") according to their energy and displayed in a spectrum as number of counts in different spectrometer channels corresponding to preset energy intervals. The detected energy values are electronically identified as electron transitions of different elements. Such an EDXS spectrum is shown in figure 3.6. It should be noted that the detection and processing steps involve statistical steps that lead to a fundamental limitation in energy resolution. Current EDXS detectors have an energy resolution of the order of 100 eV, leading to peaks with Gaussian shapes instead of sharp lines and may give rise to peak overlaps for X-rays with similar energy values. In particular, the low energy values of light-element X-rays mean a higher risk of overlap, making it difficult to distinguish the different elements. The lower characteristic X-ray yield and overlapping peaks can make it challenging to perform EDXS analysis of low Z-number materials such as OSCs. Combined with sample beam damage, which is discussed in section 3.2.5, it can be difficult to obtain reliable EDXS spectra or maps for these systems. However, modern improvements in spectrometer efficiencies and larger detector collection angles are making EDXS analysis increasingly applicable for OSCs. [19]

The intensity of each peak in an EDXS spectrum is related to the concentration of corresponding element. Thus, measuring the relative strength of each spectrum peak enables quantitative EDXS analysis. For a reliable quantification, a high peak-to-background ratio should be obtained for all characteristic peaks so that the background signal can unambiguously be subtracted. [19] After subtraction, the true intensity I of each characteristic peak can be obtained through integration. If two elements are present in the spectrum, the relative concentrations of the elements C_A and C_B can be calculated with the Cliff-Lorimer equation

$$\begin{aligned} C_A/C_B &= k_{AB} I_A/I_B \\ C_A + C_B &= 1 \end{aligned} \tag{3.1}$$

where k_{AB} is a non-constant sensitivity factor often termed the Cliff-Lorimer factor. k_{AB} depends on the elements, absorption of X-rays and X-ray fluorescence in the sample. [113] Although simple in concept, obtaining accurate k-factors can be difficult in practice. Modern EDXS software often comes with pre-determined Cliff-Lorimer factors. These are often sufficient to estimate the material composition, but highly accurate quantification may require other methods. [19, 114] Modern advancements in detectors and post-acquisition processing are constantly improving the accuracy of EDXS, which have in recent years reached the milestone of mapping chemical elements with atomic resolution. [115, 116] EDXS was performed to confirm the elemental compositions of all samples studied in this thesis,

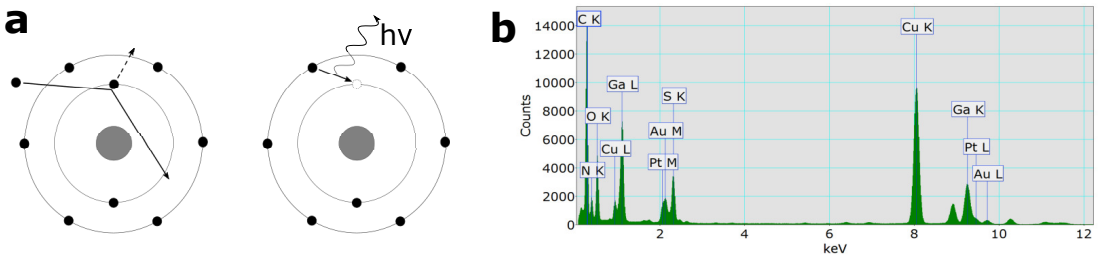

Figure 3.6: (a) Mechanism for characteristic X-ray generation: An incoming electron knocks out a sample electron from an inner electron shell. This allows an electron from an outer shell to relax to the inner shell and emit a X-ray corresponding to the relaxation energy. (b) Example of an EDXS spectrum obtained by analysing characteristic X-rays.

and was of specific importance in the study described in section 4.1.2 where EDXS mapping was used to determine the separation of components in the bilayer film.

3.2.5 Minimising Radiation Damage on Samples

Modern electron microscopes are capable of achieving an incredibly high spatial resolution, but the high-energy electron beam's interaction with the sample may cause radiation damage that will limit the analysis of the true state of the material. It is important to understand these damaging interactions in order to limit their extent, especially for soft materials like OSCs. This section will list common damage mechanisms and methods to minimise their effect.

Damage from Elastic Scattering

Elastic scattering by electrons from the primary beam and the sample atoms' nuclei may lead to so called knock-on damage. The total amount of energy is conserved in an elastic interaction, but energy can still be transfered from beam electrons to the nucleus followed by a significant change in the electron trajectory. This transferred energy may be sufficient to displace the sample atoms, permanently rearranging the structure or sputtering them away which will result in mass-loss. The displacement of sample atoms due to elastic scattering from the electron beam is referred to as knock-on damage. Knock-on damage is commonly the dominant damage mechanism during analysis of conducting materials such as metals. The effect is decreased at lower beam energies and for higher atomic weights. All atomic sites are also not affected equally by the scattering, for example a surface atom may

more easily be displaced than an atom in the bulk of a sample. The minimum energy required to displace an atom is called the displacement energy, which is dependent on atomic weight, bonding with surrounding atoms and location within the sample. A maximum transfer energy lower than the displacement energy means a drastic reduction in knock-on damage. Thus, it is possible to lower the beam acceleration voltage below certain threshold values in order to make knock-on damage negligible. [117]

Damage from Inelastic Scattering

When the incident electrons change kinetic energy due to interaction with the sample atom, it is considered inelastic scattering. This change is usually a loss in electron energy, which can vary from a few electron volts up to hundreds of electron volts and significantly affect the sample. Inelastic scattering commonly results in ionisation of sample atoms, excitation of phonons or excitation of valence- or conduction electrons in the material. Although such interactions provide useful signals that can be analysed in the microscope, they also result in radiolysis, heating and electrostatic charging, which are the dominant sources of damage for soft materials such as OSCs. [118]

Sample heating due to inelastic scattering can be problematic for materials with low thermal conductivity, and combining this with a low thermal stability may result in significant decomposition due to the local rise in temperature. Similarly, electron beam interactions may cause a build-up of charges in poorly electrically conducting materials, leading to local potential differences that may result in sample damage. Radiolysis, or ionisation damage, occurs when an exited sample atom or molecule do not return to its original electronic state upon deexcitation. This results in permanent changes in atomic or molecular structure due to breaking of chemical bonds or cross-linking between new species. Bonds between C- and H atoms are easily broken in organic samples, and the reformation of bonds prevents hydrogen from rebinding which leads to mass-loss. As opposed to knock-on damage, there is no threshold in acceleration voltage where radiolysis is significantly reduced. Instead, the effect from radiolysis increases at lower acceleration voltage, meaning that the beam energy has to be carefully selected for different samples to minimise damage from both mechanisms. The cross-section of radiolysis is several orders of magnitude higher than for knock-on damage, so although damage through elastic scattering do occur in organic samples, it tends to be dominated by inelastic effects such as radiolysis. [20] A recent study of beam sensitive phosphorene showed that radiolysis can be reduced by protective layers such as graphene. Materials like graphene can both suppress knock-on damage by acting as a net to

reduce sputtering of atoms and suppress radiolysis via fast charge transfers due to its excellent transport properties. The authors showed that encapsulating phosphorene in graphene increased the sample durability to approximately 13 times higher than the bare material. [119]

Heating and charging are direct dose rate dependent effects, meaning that the total electron dose is less important than the dose rate. Higher electron dose rates mean that heat or charges can not be transported away at a sufficient pace, leading to a rise in local temperature or electrostatic potential and eventual decomposition of the sample. For direct dose rate effects there may exist a threshold rate for when build-up occurs, so reducing dose rate below this can reduce the damage to negligible levels. For radiolysis, however, only the total dose is relevant and a larger current density over a shorter time should produce a similar amount of damage. Therefore, a critical dose, D_c, can be defined to quantitatively measure the material's sensitivity to damage. Since radiolysis in TEM can be approximated to follow first-order decay kinetics $S = S_0 e^{(-D/D_c)}$, for initial and measured signals S_0 and S at dose D, the critical dose can be determined as the dose when the signal reaches $1/e$ of its initial value. As an example, aromatic hydrocarbons usually have a higher D_c than aliphatic hydrocarbons due to resonance stabilisation of the phenyl rings. Finally, a material may also exhibit a decreased dose sensitivity for higher dose rates, *i.e.* an inverse dose rate effect. An inverse dose rate dependence favours the use of higher currents in the TEM in order to outrun damage in the sample. [20]

Secondary Damage Effects

In recent years it has been noted that D_c for conjugated polymers may first increase and then decrease as a function of dose rate, *i.e.* showing first an inverse and later a direct dose rate dependence in different dose rate regimes. It has been proposed that this behaviour can arise due to slow, diffusion limited processes from secondary reactants. As bonds are broken from radiolysis, some resulting species may start to react with their surroundings in a cascading manner that breaks down the material. These secondary processes should be diffusion limited, meaning that it is possible to outrun the damage with increased dose rate. On the other hand, too high dose rate can result in local heating, leading to an increased rate of diffusion and thus more damage. [120]

The extent of damage from secondary species is complex and not yet fully understood. It has been noted that cryogenic conditions can reduce sample damage in TEM, which could be due to suppression of atomic motion after bonds are bro-

ken or lowering the rate of diffusion for secondary reactants. A recent study has shown that damage can also be suppressed by adding antioxidants to the sample in order to neutralise reactive species before they break down the material. The study showed increased D_c for three OSCs after addition of antioxidants, even without the additives being incorporated into crystals, highlighting the importance of secondary damage processes for this type of material. The increased material stability allowed the π-stacking to be resolved in one of the OSCs, which had previously not been possible due to beam damage. [120]

3.3 TEM Sample Preparation

This section presents the sample preparation techniques used in this thesis in order to obtain high-quality OSC thin-film samples for TEM analysis. The following two methods are discussed: the float-off technique from spin coated thin-films and the lift-out technique using a combined focused ion-beam and scanning electron microscope (FIB-SEM).

3.3.1 Float-off

As discussed in section 3.1.5, spin coating is a common method to fabricate thin-film specimen of OSCs. By adding additional steps to the spin coating procedure, it can be used to prepare samples for TEM analysis. This is commonly referred to as the float-off technique, and is illustrated in figure 3.7 a-c. The float-off technique is done by spin coating a sacrificial thin-film on the substrate, and subsequently a film of the material of interest. By immersing the substrate and the two layers into a dissolving agent for the sacrificial layer, for example deionised water, the second layer will be released and can float up to the water surface. Finally, tweezers can be used to submerge a TEM grid under the floating film and then pick it up directly on the grid. After drying, the sample can then be transferred to a microscope for analysis. [121, 122] The float-off technique is the main sample preparation method used in this thesis to prepare OSC thin-films.

3.3.2 Focused Ion Beam - Scanning Electron Microscopy (FIB-SEM) Lift-out

Another method for preparing thin OSC samples for TEM analysis is through lift-out using focused ion beam - scanning electron microscopy (FIB-SEM). The

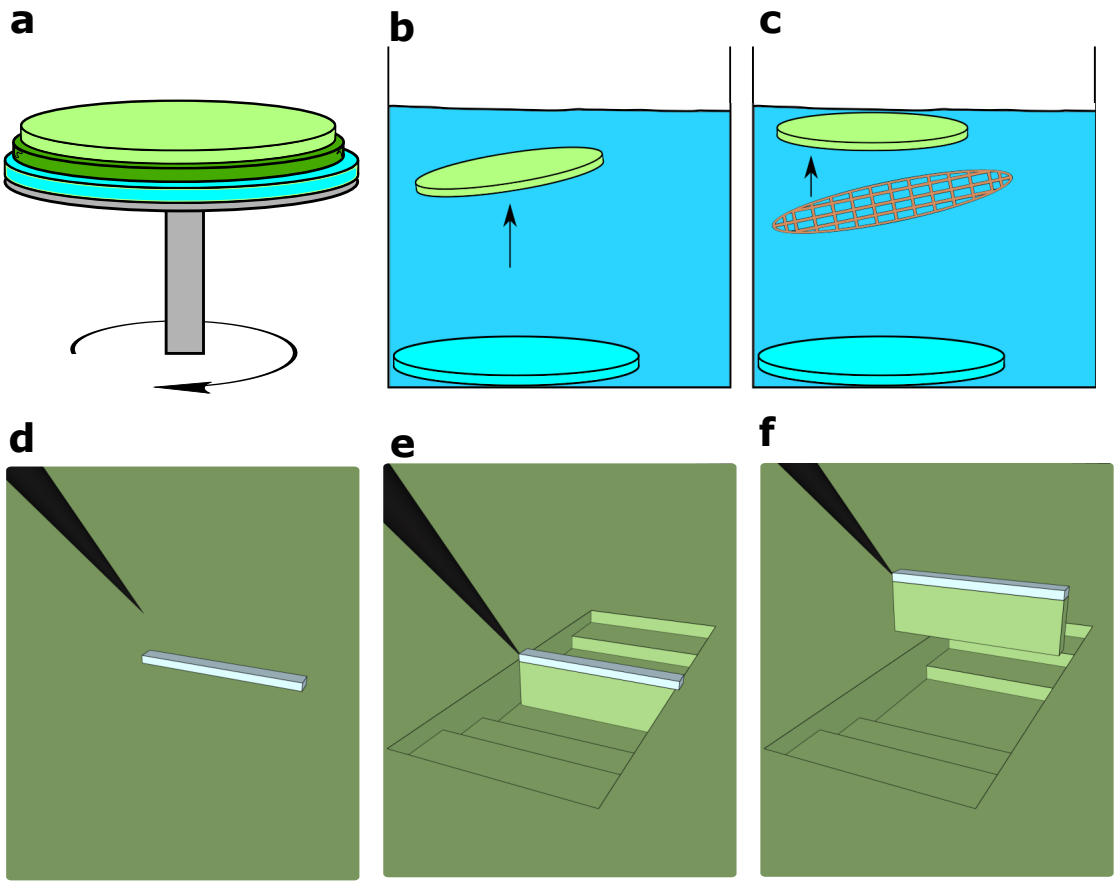

Figure 3.7: The main steps of the two sample preparation techniques: float-off and FIB-SEM lift-out. (a) Two thin films are fabricated through spin coating: a sacrificial film and the film of interest on top. (b) Immersing the substrate and the films in a dissolving agent will release the film of interest, which will float to the surface. (c) The floating film can be picked up directly on a TEM grid. (d) An area of interest is identified using a FIB-SEM and a protective layer is deposited on top. (e) The area surrounding the area of interest is milled away, freeing up a lamella of the area of interest which is welded to a micromanipulator. (f) The lamella is cut loose from the sample and lifted out to the TEM grid using the micromanipulator.

lift-out procedure is illustrated in figures 3.7 d-f. A FIB-SEM is a dual-beam instrument that combines the electron beam of a scanning electron microscope with an ion-beam that uses a similar principle. The most common choice of ion is Ga^+, meaning that the particles in the ion-beam have a significantly higher mass than those in an electron beam. After aligning the electron beam and the ion-beam in a FIB-SEM, it is possible to simultaneously use electrons to image an area and use ions to perform manipulations such as sputtering away material according to preselected patterns. Additionally, if the FIB-SEM is equipped with a metal evaporation source, commonly a gas injection system (GIS), the ion beam can be used to deposit a protective metal layer on top of selected areas in the sample. [123]

Using a FIB-SEM, it is possible to select a specific region of interest in a sample, mill out its surroundings, lift out the selected region and attach it to a TEM grid according to the following procedure. After selecting an area for lift-out, a metallic (or carbon-based) layer is deposited to protect the area from subsequent exposure to the ion beam. Using the GIS, an organometallic precursor gas is ejected over the area and decomposed using the ion beam during a predetermined time. A frequent choice of metal is Pt, where a 1 µm thick layer is normally deemed sufficient for protection. To prevent ion and Pt implantation in the material of interest, the first initial nm of protective layer may also be deposited using the electron beam. The area surrounding the protective layer is then milled away using the ion beam, forming a thin slice, *i.e.* a lamella. By tilting the sample relative to the ion beam, the area underneath the lamella may also be milled away at a chosen depth. Before completely cutting loose the lamella, a needle-shaped micromanipulator is inserted until it is barely touching the sample, and the lamella is welded to the micromanipulator using the GIS. The lamella is cut loose and moved to a TEM grid, which it is welded to and removed from the micromanipulator. After being securely welded to the TEM grid, final thinning is carefully performed on the lamella to make it sufficiently thin for TEM analysis. The lamella can be rotated 90° during the transfer to the TEM grid, meaning that the in-plane orientation in the TEM will be a cross-section of the sample. Due to this, FIB-SEM lift-out is an excellent method to prepare cross-sections for analysis of depth profiles. [123]

Comparing FIB-SEM lift-out to spin coating and float-off as a sample preparation technique for OSCs, lift-out using FIB-SEM offers the advantage of selective analysis over an area of the researcher's choice, and lift-out is necessary if analysis of a cross-section is required. However, it is a time-consuming sample preparation technique and the resulting samples are small, which may introduce an operator bias when studying the material. Also, thinning soft materials such as OSCs to only a few tens of nanometers can be difficult in a FIB-SEM, meaning that the

thickness of the spin-coated sample has the potential to be lower. [124] Ultimately, there are advantages and disadvantages of both methods and the choice of sample preparation technique is often determined by the type of analysis that will be performed on the material. In this thesis, the FIB-SEM lift-out technique was used to create cross-section samples of the bilayer film discussed in section 4.1.2.

4 Results and Discussions

This chapter shows and discusses the results from the electron microscopy studies of OSC systems, and their correlation to device-relevant properties. Two different principal types have been studied. The first is a blend, and the other one is a doped structure. The mechanisms enabling the tuning of the properties are different between the two types of structures. Section 4.1 focusses on OSC blends, and how nanoscale constituents determine the blends' electrical and mechanical properties. Section 4.2 focusses on doped semiconducting polymers. The 2D and 3D dopant distribution characteristics is visualised with sub-nanometre resolution, and the effect of changes in chemical structure is determined. The studies show that it is important to extract the 3D distribution. Subsequently, this is correlated to the electrical properties of the materials in section 4.3. The results presented in this chapter provide insights in how structural changes determine the material properties of OSCs.

4.1 OSC Blends

This section presents nanoscale constituents in OSC blends that are studied using a combination of high-resolution TEM imaging and spectroscopy. Important aspects are aggregation characteristics, interface structure and phase distribution. The work is published in papers I, II and III. The systems of interest are thin-films of the copolymer p[p($g_4$2T-T)-co-U] and neat p($g_4$2T-T), a bilayer structure of BBL and p($g_4$2T-T) and a BHJ of TQ1:$PC_{71}BM$.

4.1.1 Aggregation Characteristics of Copolymer p[p($g_4$2T-T)-co-U]

Section 2.3.2 mention that practical application of TEGs requires thermoelectric materials with suitable electrical and mechanical properties. Optimal mechanical properties are a balance between sufficient flexibility to deform without fractures and sufficient robustness to form free-standing films. For this purpose, the synthesis of a material consisting of p($g_4$2T-T) blocks and hard linker segments of

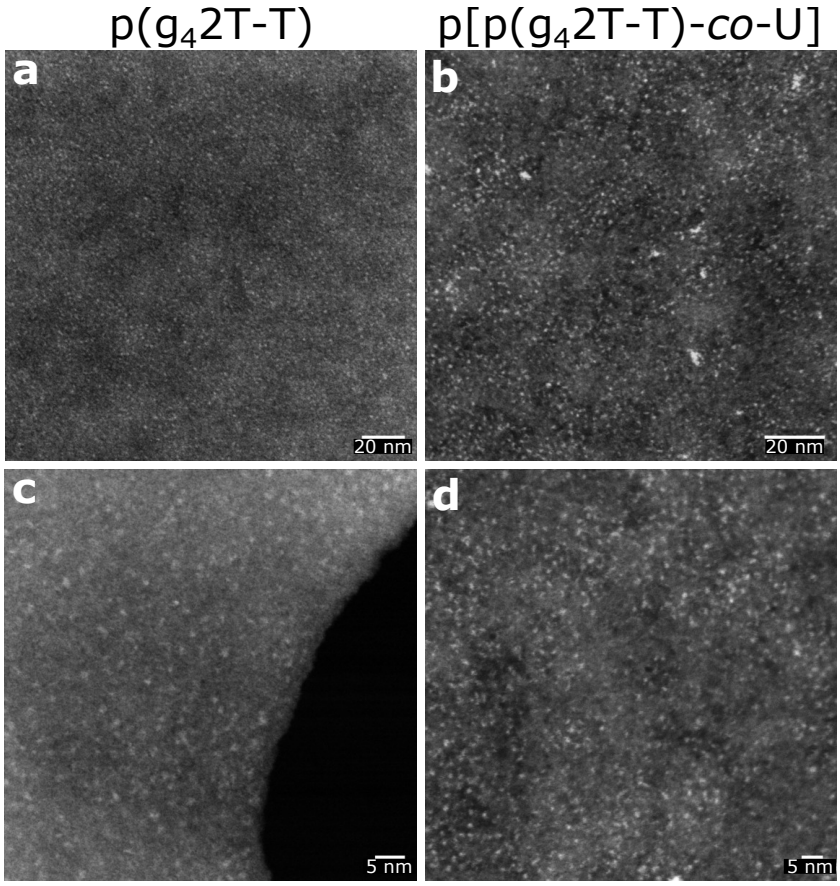

Figure 4.1: HAADF-STEM images of (a, c) p($g_4$2T-T) and (b, d) p[p($g_4$2T-T)-co-U]. Both neat polymer and the copolymer display the same granular texture but lacks large aggregations, indicating that the urethane units are introduced without significant disruption of the p($g_4$2T-T) nanostructure.

urethane is reported in paper I. High resolution STEM was performed on the resulting copolymer p[p($g_4$2T-T)-co-U] and compared to neat p($g_4$2T-T) in order to study the nanostructure of the materials. Samples of p($g_4$2T-T) and p[p($g_4$2T-T)-co-U] were fabricated through the spin coating and float-off method described in section 3.3.1, resulting in thin-films that were picked up on TEM grids and transferred to the microscope for imaging. Analysis in HAADF-STEM mode at 300 kV resulted in the images shown in figure 4.1.

In this figure, it can be seen that both materials contains bright features of single-nanometre sizes across the film. These features may form as a result of micellar-like structures that have previously been inferred for pure p($g_4$2T-T). [67] Distinct do-

mains of urethane blocks, approximately 5 nm long, were expected in the copolymer. These should be discernible due to their denser and more ordered structure, but could not be resolved during the analysis. A possible reason for this could be that the domains are distributed evenly in all three dimensions, making it difficult to distinguish them in projection in samples where multiple blocks may be overlapping. Importantly, no large aggregations of the different components can be observed in these images. The lack of aggregates indicate that the urethane units are successfully added to the p($g_4$2T-T) without any significant disruption in the polymer nanostructure. Complimentary measurements show that the successful inclusion of the urethane segments only leads to a slight reduction of electrical properties but a significantly enhanced robustness for the copolymer. This robustness is sufficient to form a free-standing solid, which makes the copolymer p[p($g_4$2T-T)-co-U] a promising material for applications such as for the active material in thermoelectric generators.

4.1.2 Interface Structure of Bilayer p($g_4$2T-T):BBL

Sections 2.1.2 and 2.2 discuss that the difficulties in controlling the position of molecular dopants may lead to low long-term stabilities and eventual loss of performance due to dopant aggregation. Ground-state charge transfer presents a way to ignore the drawbacks of adding dopants by instead matching the levels of ionisation energy and electron affinity of two OSC components in a system. Upon physical contact, an electron transfer will then occur spontaneously between the components in the electronic ground-state without any external stimuli, resulting in an interface that can act as a charge transport layer. The study in paper II reports the first time a ground-state charge transfer has been observed for an all-polymer system by combining the polymers p($g_4$2T-T) and BBL. The contact between the polymers resulted in a quasi-two-dimensional interface with a drop in electrical resistance of several orders of magnitude compared to that of the pure polymers. Kinetic Monte Carlo (KMC) simulations indicate that the charge transport is confined to a narrow interface between the components that is only a few nanometres wide. Thus, a sharp interface between the polymers is crucial in order to form a continuous highly conductive transport layer through the material. Bilayer films were prepared for electron microscopy study by spin coating the p($g_4$2T-T) and BBL on a gold electrode. In order to image the depth profile and the interface of the bilayer, cross-sections had to be prepared from the sample using the FIB-SEM lift-out scheme presented in section 3.3.2. The TEM lamella produced from the lift-out was transferred to a TEM to be imaged using HAADF-STEM at 200 kV, revealing the structure illustrated in figure 4.2.

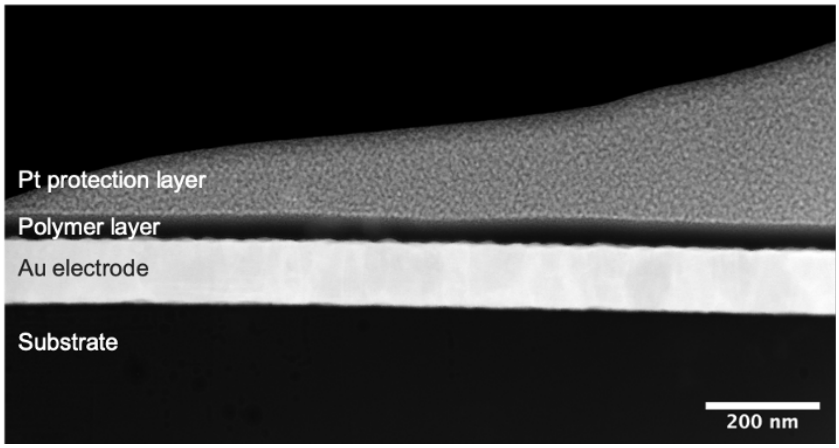

Figure 4.2: 200 kV ADF-STEM image showing the different layers of the spin coated bilayer p($g_4$2T-T):BBL on a Au electrode. A protective layer of Pt was deposited on top of the polymers.

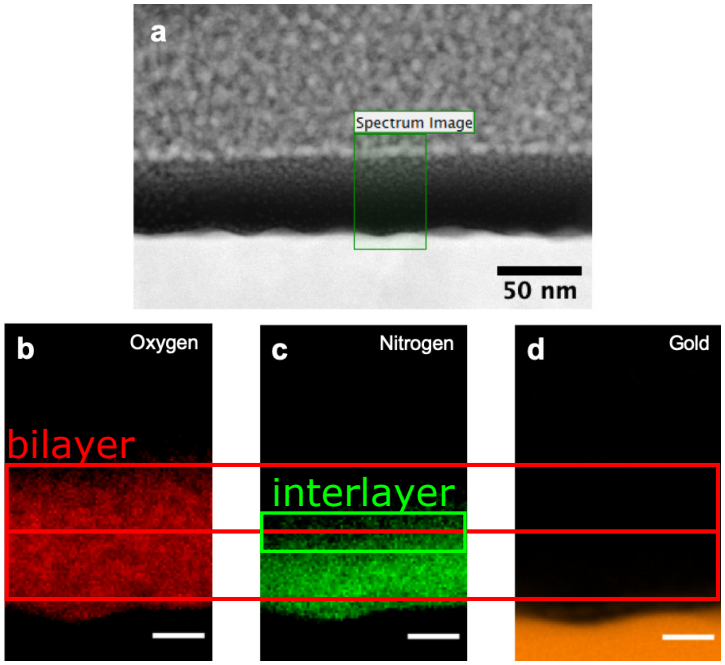

Figure 4.3: EDXS mapping of the oxygen and nitrogen distribution in bilayer p($g_4$2T-T):BBL, at 200 kV. (a) ADF-STEM image of the bilayer. The area for EDXS analysis is marked "Spectrum Image". (b) Oxygen map. (c) Nitrogen map. (d) Gold map. Scale bars in (b)-(d) are 10 nm.

A clear layered structure is visible in the figure, where the interfaces between substrate, gold electrode, polymer layer and the platinum protection layer from the lift-out procedure are clearly visible. However, the low contrast of the two polymer layers made it difficult to distinguish their interface directly through HAADF-STEM imaging. Instead, the chemical differences was utilised by performing EDXS-SI by acquiring an EDXS spectrum for each pixel in a designated area, resulting in the data displayed in figure 4.3. The maps displaying the distribution of chemical elements in area indicate the presence of oxygen in the entire polymer layer, while nitrogen only is present in the lower part. Since nitrogen is a component of BBL but not of p($g_4$2T-T), this proves that the polymers remain separated in the bilayer. Furthermore, the signal from nitrogen ends sharply, with an interlayer that is only a few nanometres wide. These results experimentally confirm that a continuous transport layer can form at the polymer interface due to ground-state charge transfer. The highly conductive interfacial regions were maximised by blending the two polymer components into a BHJ, resulting in a bulk conductivity four to five orders of magnitude higher than that of the pure polymers.

4.1.3 Phase Distribution Data of TQ1:$PC_{71}BM$ BHJ for Simulations

Accurate simulations are crucial for the understanding and development of novel materials for organic electronics. KMC has proven to be a powerful tool to study the charge carriers dynamics for OPVs, but has had difficulties to correctly simulate the current voltage (J-V) curve under illumination. Modelling the J-V curve is important since it is a key part of describing the performance of an OPV. A solution to this problem is presented in paper III by calibration of a KMC model using real experimental data. A main result of this study is that realistic data of the nanostructure is required in order to take into account recombination effects that may occur due to the phase distribution. For this purpose, electron microscopy analysis was performed on a BHJ of the polymer TQ1 and the fullerene $PC_{71}BM$. Free-standing thin-films were prepared on TEM grids using the spin coating and float-off method described in section 3.3.1. BF-TEM imaging at 200 kV revealed a granular structure with low contrast regions approximately 100 nm in size seen in figure 4.4. These low contrast regions were attributed to fullerene-rich domains due to their higher density.

However, since diffraction contrast from crystalline regions can make it difficult to interpret BF-TEM images with certainty, complimentary HAADF-STEM imaging was also performed on the same sample at 300 kV. The similar structures seen

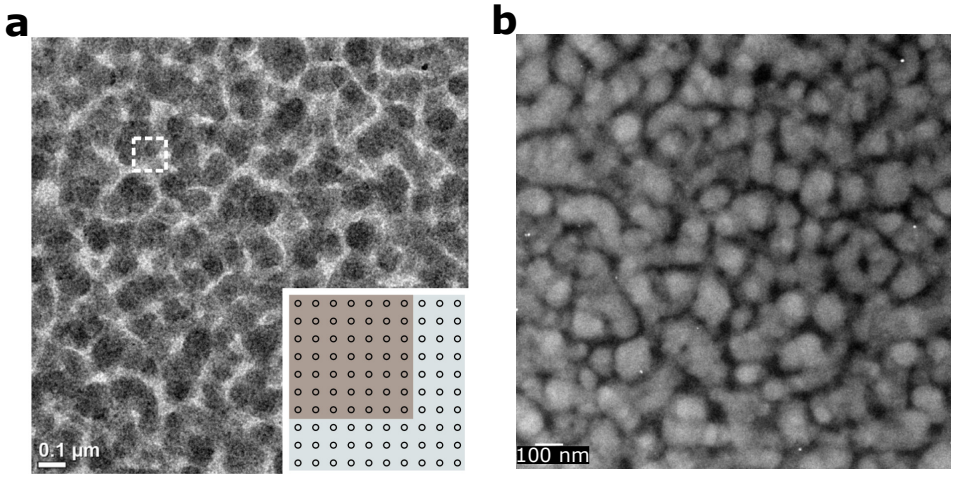

Figure 4.4: Phase distribution of TQ1:$PC_{71}BM$. (a) BF-TEM image of a TQ1:$PC_{71}BM$ BHJ and (b) complimentary HAADF-STEM imaging on the same sample. Inset in (a) shows a numerical implementation of the nanostructure for the KMC model, taken from the dashed square in the image. $PC_{71}BM$ aggregates are assumed as 7 x 7 inclusions in a 10 x 10 unit cell representing the mixed component phase.

with an inverted contrast in figure 4.4 indicate that the observed features are correctly interpreted as aggregates of the fullerene $PC_{71}BM$. The data of the blend phase distribution acquired from the electron microscopy images were included in the KMC models in order to tune the recombination yields to more realistic rates. The calibrated model was able to fully describe the J-V curve of a disordered OPV under illumination of light. The results from this study highlights the importance of collaborative work between theoretical simulations and data acquired from experimental observations in order to investigate and improve future materials for organic electronics.

4.2 Doped Semiconducting Polymers

As discussed in section 2.1.2, doping using molecular dopants is a promising method to control the properties of OSCs. The nanoscale distribution of molecular dopants is important for their efficiencies. TEM has the potential for a sufficiently high resolution to directly visualise this distribution. However, many types of OSCs and molecular dopants contains elements of similar atomic number, resulting in a low contrast between the components. This section presents and discusses the results from papers IV and V, which address the low average Z-

number OSC p(g_x2T-T) doped with the high average Z-number molecular dopant Mo(tfd-$COCF_3$)$_3$. The focus of paper IV is the effect of dopant concentration in p($g_4$2T-T). Paper V extends this analysis to the effect of side-chain length, adding p($g_3$2T-T) and p($g_6$2T-T), which reveals how this modification in chemical structure directly impacts the dopant distribution.

4.2.1 Visualising 2D Dopant Distribution of Mo(tfd-$COCF_3$)$_3$ in p(g_x2T-T)

Mo(tfd-$COCF_3$)$_3$ doping of p($g_4$2T-T) was performed by the mixed-solution method. Thin-film samples were prepared according to the spin coating and float-off method explained in section 3.3.1, yielding free-standing TEM samples. The dopant concentrations were 5 mol%, 20 mol% and 40 mol%, respectively. Figure 4.5a shows HAADF-STEM images of the nanostructure of the analysed samples. The high average Z-number of Mo(tfd-$COCF_3$)$_3$ ($\approx$ 20.0) compared to p($g_4$2T-T) ($\approx$ 7.7) results in a significant Z-contrast in HAADF-STEM mode. Thus, the high contrast features seen in the figure are assumed to be dopant species that are imaged directly. EDXS analysis was also performed over larger areas, which confirmed that Mo was the only high Z-number element present in the samples. Imaging dopants directly, without the use of spectroscopy techniques, allows for a dose-efficient determination of the dopant positions without significant structural damage. However, it is difficult to draw conclusions regarding the dopant distribution at different concentrations based on the images in figure 4.5a. Since imaging in transmission yields 2D projections of samples that in reality are 3D, features may overlap in the direction parallell to the incident electron beam. The complete dopant distribution in these samples can not be visualised in 2D. The limitations of 2D TEM imaging was overcome by performing electron tomography on all samples, which is described in the following section.

4.2.2 Visualising 3D Dopant Clustering of Mo(tfd-$COCF_3$)$_3$ in p(g_x2T-T)

As explained in section 3.2.3, a 3D tomographic reconstruction can be obtained by acquiring a tilt series of HAADF-STEM 2D projections of a sample volume. Such tilt series were acquired for the doped OSC samples described in section 4.2.1 and used to reconstruct the volumes. The analysed regions were imaged before and after each tilt series to confirm that no significant structural damage had occurred during acquisition. The tilt series for all reconstructions used a Saxton scheme and

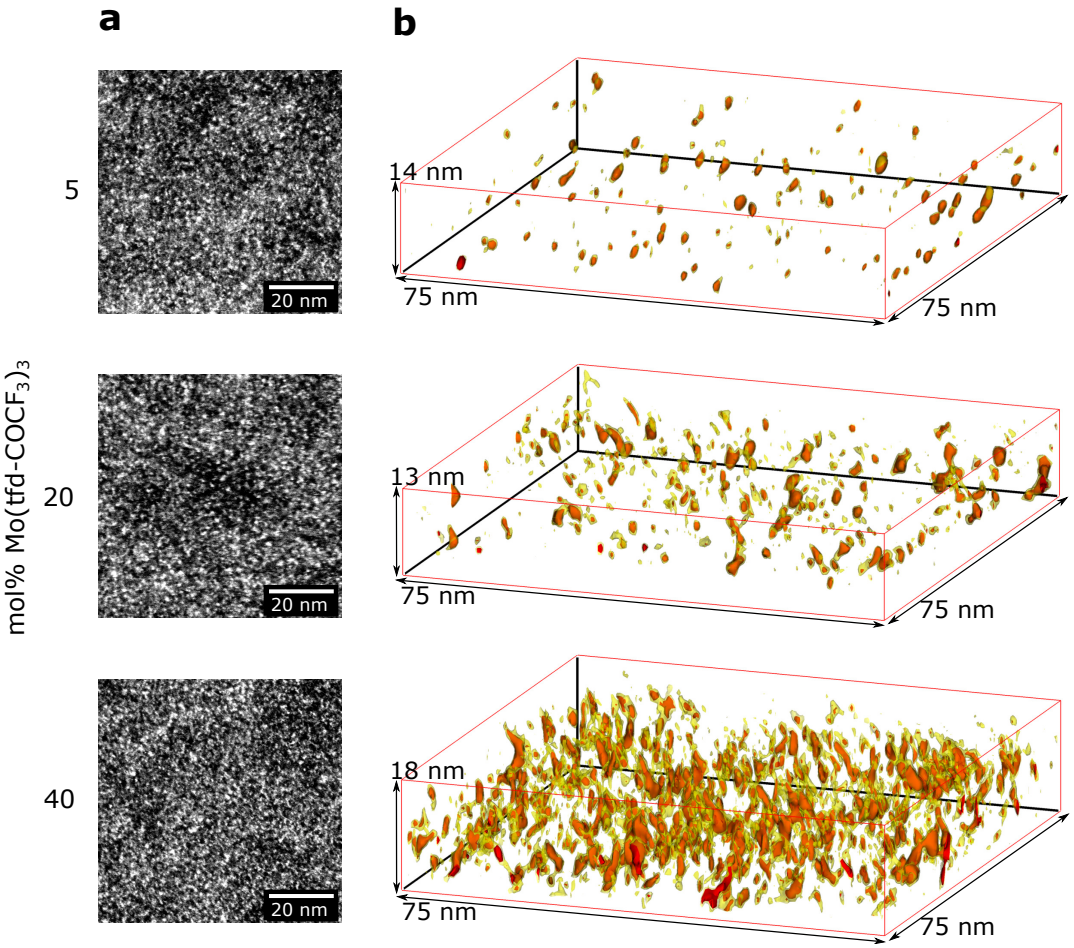

Figure 4.5: p($g_4$2T-T) thin-films doped with 5, 20 and 40 mol% Mo(tfd-$COCF_3$)$_3$. (a) 300 kV HAADF-STEM images of representative areas. The high intensity features are direct visualisations of the dopants. (b) Electron tomography reconstructions based on HAADF-STEM tilt series. Red intensity thresholds represent the position of dopant species and yellow intensity thresholds represent the dopant pendant groups.

spanned angles between -70° and $+70^{\circ}$ with a 2.5° step at the 0° angle, resulting in 79 images for each series. The SIRT algorithm described in section 3.2.3 was used for the reconstruction and iterated 25 times for each sample in order to minimise background noise. The resulting volumes are shown in figure 4.5b.

The spatial resolution of the tomography experiments was carefully tuned to enable the 3D positions of individual dopant species to be resolved. The voxel side length in the reconstructions is 0.5 nm, while the dopants are approximately 1.2 nm along the long axis and 0.6 nm along the short axis. [60] A volume equivalent to an in-plane area of 2 600 μm^2 was reconstructed and analysed for each sample in order to confirm that the reconstructions shown in figure 4.5b were representative of the material. The red intensity thresholds in figure 4.5b were set at a high value, and represents the position of the dopant species. A fine-calibration of the red intensity thresholds were performed relative to each other to retain a 5:20:40 ratio between voxels representing dopants for the 5, 20 and 40 mol% samples. The yellow intensity thresholds were set at a slightly lower value, and are generally located around the red intensity regions. They are interpreted to correspond to the fluorinated pendant groups of the dopant, which are expected to yield a slightly higher signal compared to the surrounding OSC but lower than the central part of the dopant specie. The presence of lower intensity regions surrounding the high intensity can be explained by conformational changes of the pendant groups during the tilt series acquisition. The volume of the high-intensity regions reflects the number of dopants present at each high-intensity region. The position of individual dopant species can be shown in the reconstructions. This is illustrated in figure 4.6, where each dopant specie is indicated with a purple marker. The diameter of the marker is 1.2 nm, which corresponds to the longest axis of the dopant specie. [60] Due to the small number of species in the clusters, it is possible to mark the position of each individual dopant in the clusters.

The reconstructed volumes show a significant difference in 3D dopant distribution between the three samples. The results show that the dopants have a preference to form clusters in the systems. The majority of the high-intensity regions in the reconstructed volumes are larger than the size of one dopant specie, indicating that the dopants have a preference to form clusters in the systems. Comparing the different samples, a trend of increasing cluster size with increasing dopant concentration can be observed. Additionally, the cluster morphology changes to an increasingly elongated shape and the distance between clusters decreases with increasing dopant concentration.

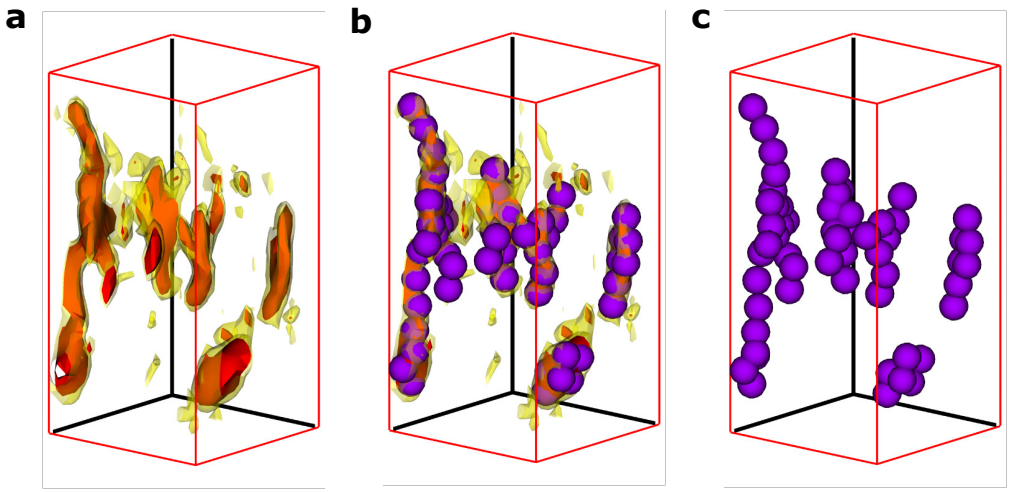

Figure 4.6: Fitting markers to a tomography reconstruction in order to indicate the position of individual dopant species. The markers are spheres with a diameter of 1.2 nm, which corresponds to the longest axis of the dopant specie. (a) A reconstructed sub-volume. (b) Markers are fit to the high-intensity voxels of the reconstruction. (c) The high-intensity regions are removed, leaving only the markers in the sub-volume.

4.2.3 Dopant Distribution and OSC Side-chain Length

Section 2.2.3 discusses that there have been previous attempts at controlling the dopant distribution by modifying the side-chains of semiconducting polymers. Varying the side-chains may impact dopant incorporation, resulting in changes in the final dopant ordering. There have been previous reports of studying the effect of different apolar side-chain lengths for semiconducting polymers. [65,66,125] However, to the best of our knowledge, the effect of varying polar side-chain lengths has not been studied for semiconducting polymers such as p(g_x2T-T). The relatively simple structure of p(g_x2T-T), consisting of a polythiophene backbone and oligoethylene glycol side-chains, can be seen as a model polymer for polar side-chains comparable to how P3HT is used for apolar side-chains. Therefore, the characterisation procedure described for p($g_4$2T-T) in sections 4.2.1 and 4.2.2 was repeated for different side-chain lengths in order to study its impact on dopant distribution. p($g_3$2T-T) and p($g_6$2T-T) were selected as short and long side-chain variants. Multiple thin-film samples were prepared at dopant concentrations of 5, 20, 40 and 60 mol% Mo(tfd-$COCF_3$)$_3$ for both polymer variants. SEM imaging was performed to ensure sample quality and that the films studied using TEM were representative. These samples were imaged using HAADF-STEM and tilt series were acquired for tomography reconstructions using the method previously

described for p($g_4$2T-T). Due to the large number of samples from this analysis, figure 4.7 shows smaller sub-volumes from the reconstructions of each combination of polymer variant and dopant concentration.

The results shown in figure 4.7 indicate that the dopant cluster morphology in p($g_3$2T-T) and p($g_6$2T-T) follows the same trends as in p($g_4$2T-T) with respect to changes in dopant concentrations. However, the effect of increasing cluster volume and increasingly elongated shapes with increased dopant concentration is more severe for the long side-chain variant p($g_6$2T-T). This is more apparent if the position of individual dopant species are indicated in the reconstructions, see figure 4.7. Inspecting the markers in the reconstructions, it is apparent that the average number of dopants per cluster increases with increasing dopant concentration and that this average number is higher for p($g_6$2T-T) compared to p($g_3$2T-T). For example, the majority of the clusters in the 5 mol% samples consists of only a few dopant species, while the clusters in the 60 mol% samples are significantly larger. In order to study this trend quantitatively, data analysis was performed using scripts written in the software MATLAB.

4.2.4 Quantitative Evaluation of Dopant Distribution

All dopant clusters in the reconstructed volumes were quantitatively evaluated using MATLAB scripts. This procedure is described in detail in papers IV and V. Evaluating the data using MATLAB scripts has the advantage that a large number of clusters can be analysed for each sample, leading to values with more statistical significance. Three quantities were evaluated: the cluster volume, the aspect ratio (*i.e.* the ratio between the longest and shortest axis of the clusters) and the nearest-neighbour distance between clusters. The average values obtained from the different samples are shown in figure 4.8.

These results confirm the trends that are visually observable in the reconstructions. Figure 4.8a shows that the average cluster volume of doped p($g_3$2T-T) increases from 1.7 nm^3 at 5 mol% to 3.7 nm^3 at 60 mol%. The corresponding trend is more significant for doped p($g_6$2T-T), where the average cluster volume increases from 1.6 nm^3 at 5 mol% to 6.7 nm^3 at 60 mol%. Since each sample contains clusters that are deviating from average values, the corresponding histograms were also extracted. The relative frequencies of the different values are shown in figure 4.9. The histograms show that some dopant clusters in each sample may significantly deviate from the average values. As an example, clusters larger than 15 nm^3 can be observed for both polymer variants.

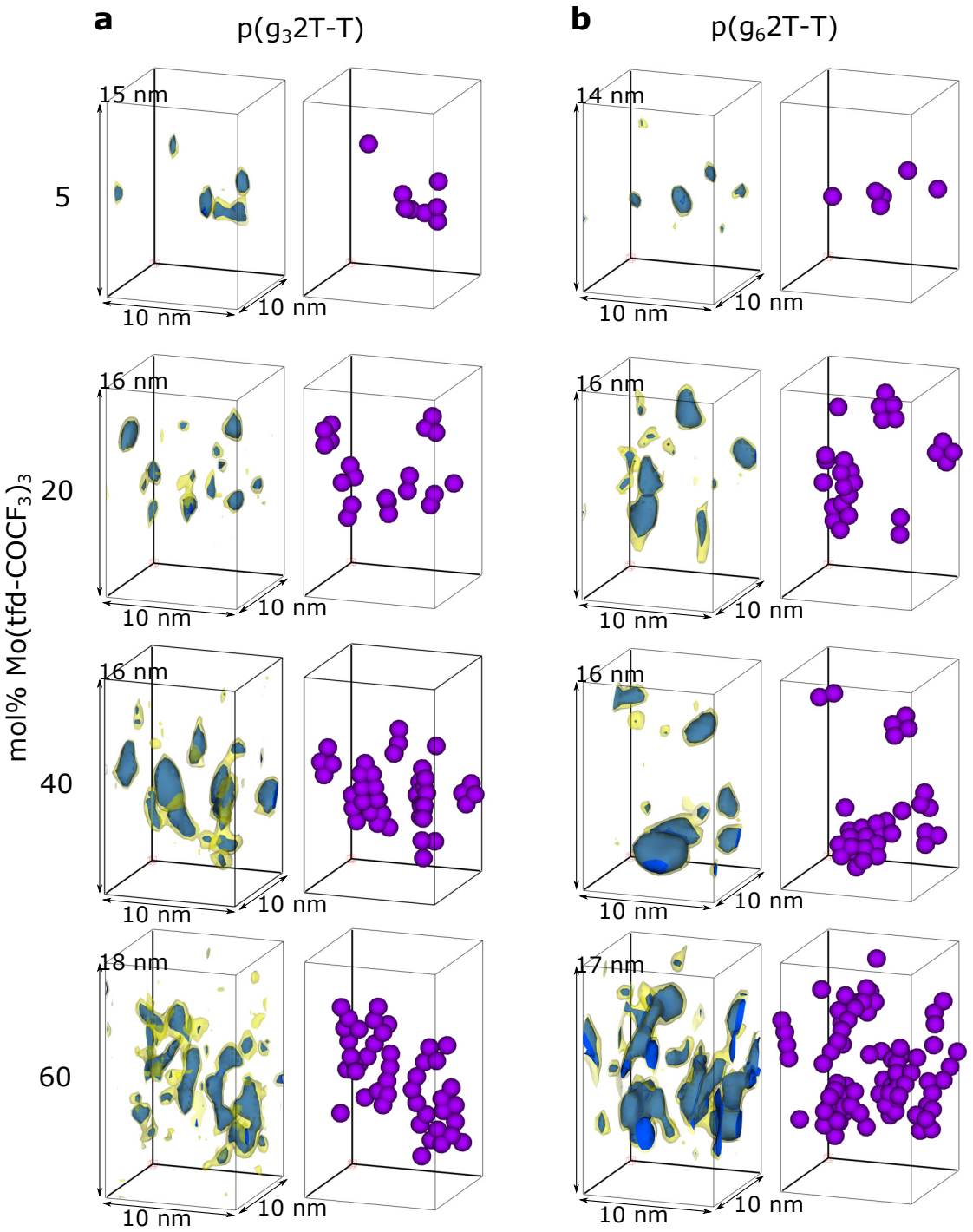

Figure 4.7: Representative sub-volumes from tomographic reconstructions of (a) p($g_3$2T-T) and (b) p($g_6$2T-T) doped with Mo(tfd-$COCF_3$)$_3$. The reconstructions are displayed as blue and yellow intensity thresholds. Blue is a higher threshold which represents the position of dopant species. Yellow is a lower threshold which represents the dopant pendant groups. Purple markers indicate the positions of dopant species in the clusters.

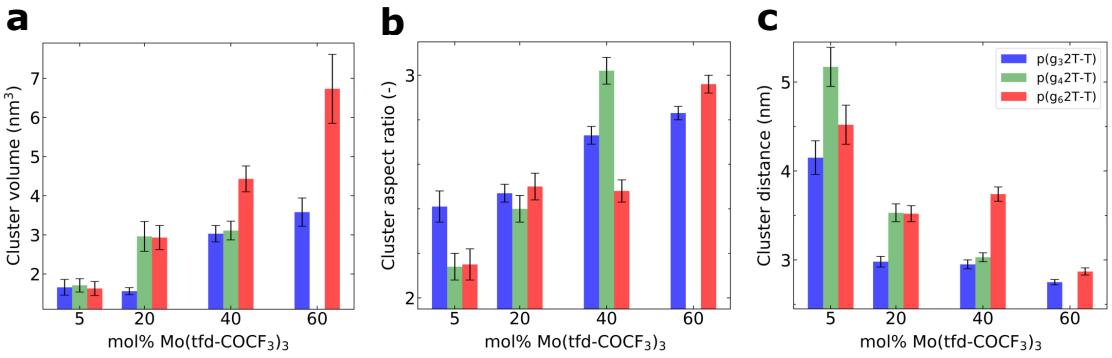

Figure 4.8: Average values of dopant cluster (a) volume, (b) aspect ratio and (c) nearest-neighbour distance. The quantification is based on tomography data of $Mo(tfd\text{-}COCF_3)_3$ doped $p(g_32T\text{-}T)$, $p(g_42T\text{-}T)$ and $p(g_62T\text{-}T)$.

Figure 4.8b shows that the aspect ratio increases with increasing dopant concentration for all samples, resulting in more elongated cluster shapes. Aspect ratios are comparable between $p(g_32T\text{-}T)$ and $p(g_62T\text{-}T)$, although slightly higher average values are measured for $p(g_62T\text{-}T)$. The aspect ratio histograms in figure 4.9 reveal multiple peaks with high relative frequency, indicating that some configurations are preferred over others. An aspect ratio of approximately 2 is common for low dopant concentrations, while a value closer to 3 appears more frequently for higher concentrations. It should be noted that features in electron tomography reconstructions can be elongated due to the missing wedge of information as described in section 3.2.3. However, the tilt series parameters described in section 4.2.2 leads to an elongation factor of < 1.3 [111], while the majority of the aspect ratios determined in the quantification have significantly higher values. An elongation factor of < 1.3 can not result in the distribution of different aspect ratios observed in figure 4.9. Additionally, the missing wedge artefact should produce an elongation directly aligned along the out-of-plane direction of the thin-films, while a significant fraction of the clusters observed in figures 4.5 and 4.7 are tilted a few degrees away from this axis. Although artefacts from the missing wedge cannot be completely excluded, it can only lead to minor contributions to the quantitative values of the aspect ratios but not affect the trends and the conclusions discussed here.

The dopant distribution is considerably heterogeneous and the nearest-neighbour distance between clusters does not change linearly with dopant concentration. In figure 4.8c, it can be observed that the nearest-neighbour distance reduces quickly with increasing dopant concentration down to a value of approximately 3 nm, and then levels off. In the histograms, a trend of wider distribution in cluster

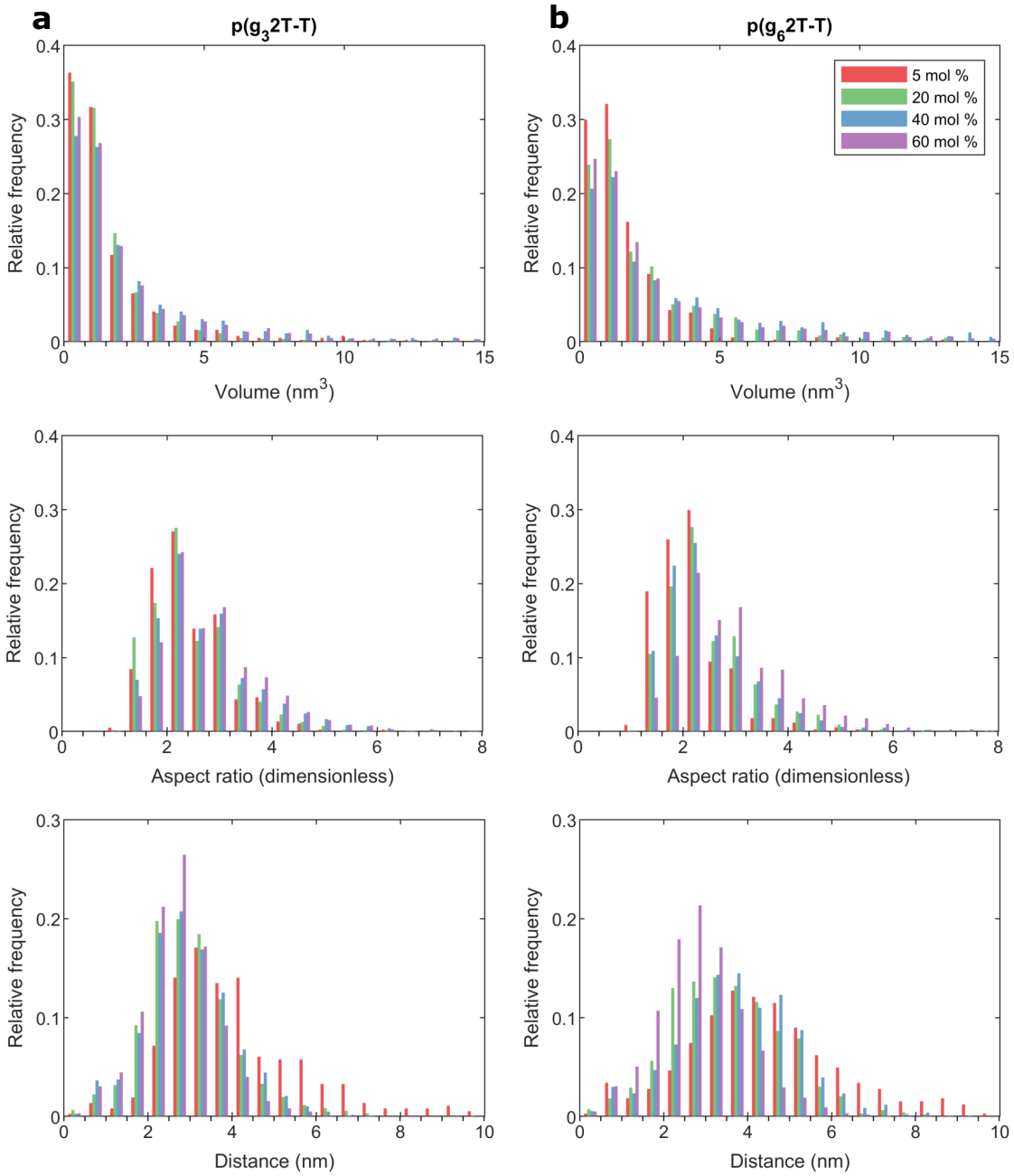

Figure 4.9: Histograms of the distributions in dopant cluster (a) volume, (b) aspect ratio and (c) nearest-neighbour distance, based on tomography data of p($g_3$2T-T), p($g_4$2T-T) and p($g_6$2T-T) doped with 5, 20, 40 and 60 mol% Mo(tfd-$COCF_3$)$_3$.

volumes and aspect ratios can be observed with increasing dopant concentration. For nearest-neighbour distance, however, the distribution gets more narrow as the dopant concentration increases. This may indicate that a minimum nearest-neighbour distance is approached at high dopant concentrations, which possibly contributes to the changes in cluster size and aspect ratio at these concentrations.

Although the theoretical assumption of a homogeneous dopant distribution is sometimes made for charge-transport simulations of OSCs [126], the results from the quantitative evaluation here show that the real distributions can deviate significantly from this theoretical assumption. Therefore, the experimental data can contribute to more realistic simulations, potentially improving the accuracy of the models.

4.3 Correlating Dopant Distribution and Electrical Properties

In this section, the electrical properties of the doped samples in paper IV and V are evaluated. The evaluation is repeated for the different side-chain lengths of p(g_x2T-T) and the different Mo(tfd-$COCF_3$)$_3$ dopant concentrations. The measurements are focused on two properties relevant for device application: electrical conductivity and optical properties. A correlation between the dopant distribution and the optoelectrical properties of the samples is observed and its implications are discussed. The relationship between chemical structure, dopant distribution and optoelectrical properties which is discussed in this section suggests additional possibilities of controlling the dopant clustering to fine-tune the performance of organic electronics.

4.3.1 Thin-film Electrical Conductivity

Molecular dopants are generally added to OSCs in order to tune energy levels and enhance electrical properties such as conductivity for the material. Thus, the effect of the dopants was analysed by performing four-point probe conductivity measurements on all doped thin-film specimens. Results from these measurements are shown in figure 4.10.

Several aspect of these results are important. Starting with p($g_3$2T-T), the conductivity initially increases as the dopant concentration increases. This effect, however, is reduced at higher dopant concentrations and a plateau in conductivity

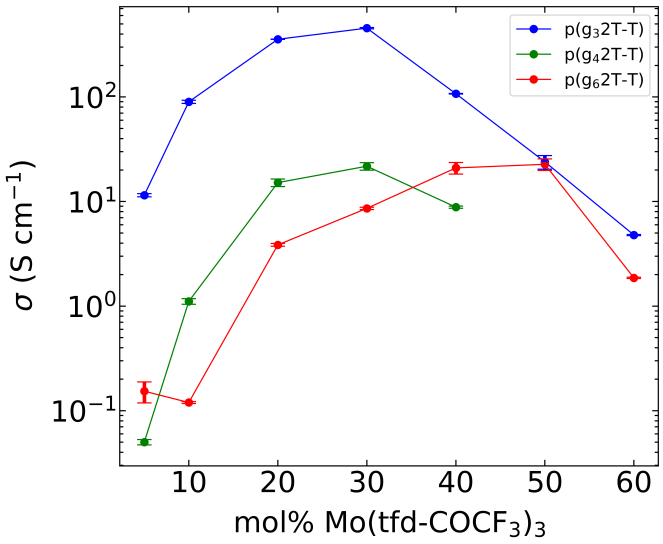

Figure 4.10: Results from four-point probe conductivity measurements on thin-films of doped p($g_3$2T-T), p($g_4$2T-T) and p($g_6$2T-T).

is observed at 30 mol% dopant concentration. After this point, further increasing the dopant concentration results in a decreased conductivity. This general trend can be observed for all polymer variants, but while p($g_4$2T-T) also has its maximum conductivity at 30 mol% concentration, p($g_6$2T-T) requires a higher concentration (50 mol%) to reach maximum. The absolute values reached are also significantly lower for the longer side-chain variants, where the maximum conductivity of p($g_3$2T-T) is approximately 20 times higher than that of p($g_6$2T-T) (455 S cm^{-1} compared to 22.7 S cm^{-1}).

Interestingly, changes in cluster morphology occurs at the same dopant concentrations as the conductivity maxima for the polymers. In figure 4.8, a notable increase in average cluster volume can be observed between 20 mol% and 40 mol% for p($g_3$2T-T), while the most significant increase for p($g_6$2T-T) is between 40 mol% and 60 mol%. Additionally, the average cluster aspect ratio increases significantly between 20 mol% and 40 mol% for p($g_3$2T-T), and between 40 mol% and 60 mol% for p($g_6$2T-T).

As discussed in section 2.2, the conductivity saturation trend in figure 4.10 has been observed in previous studies, and has been attributed to disruptions in nanostructure. [53, 54] Nevertheless, combined with the electron microscopy data, conclusions regarding a disrupted nanostructure due to dopant aggregates are not straightforward. The tomography results show that the clusters are generally only

a few nanometres in size. Additionally, the markers in figure 4.7 indicate that the clusters are sufficiently small, and have sufficiently elongated shape, to not spatially block each other from surrounding polymer chains. This means that even at high dopant concentrations, the dopant clustering should not spatially prevent charge transfer from occurring to adjacent host states. However, it is mentioned in section 2.2.2 that recently published simulations indicate how even small clustering of dopants can lead to a notable effect on electrical properties. [34] The simulations show that changing the number of dopants per cluster from 1 to 6 leads to a significantly wider density of states distribution, indicating a higher energetic disorder in the system which in turn negatively affects the conductivity. Since the clusters observed in the tomography reconstructions can be larger than 6 species, and there are also large deviations in dopant sizes, the energetic disorder is expected to be severe at high dopant concentrations.

The increase in energetic disorder could provide an explanation for the general decrease in conductivity at high dopant concentrations. However, increased energetic disorder does not offer an explanation for the differences between the polymer variants. Equation 2.1 in section 2.1.3 describes the general formula used to calculate conductivity as $\sigma = q\mu n$. Since the elementary charge q is a constant, this formula implies that changes in electrical conductivity σ can either be due to changes in charge mobility μ or due to changes in charge density n. Therefore, the charge mobility and charge density were studied in greater detail in order to understand the origin of the differences in conductivity.

4.3.2 Dopant Ionisation Efficiency and Electrical Species

Optical properties were measured by performing UV-Vis-NIR absorption spectroscopy and FTIR measurements on all samples. By combining results from both techniques, absorption from a wide range of energies could be probed. Spectra from the combined techniques are shown in figure 4.11.

Figure 4.11a reveals that the dominating spectral feature for neat p($g_3$2T-T) is a peak at 2.1 eV, which corresponds to the HOMO-LUMO transition for the polymer. As dopants are added to the system, this peak is increasingly quenched in favour of new peaks appearing. These spectral changes imply that doping successfully introduces new states to the system. At 5 and 20 mol% dopant concentrations, new peaks are emerging at 0.5 and 1.4 eV. Peaks at lower energies than the initial HOMO-LUMO transition indicate new states being added to the energy gap, *i.e.* polaron states. The increasingly pronounced polaronic bands at higher dopant concentrations indicate successful charge transfer even at higher concen-

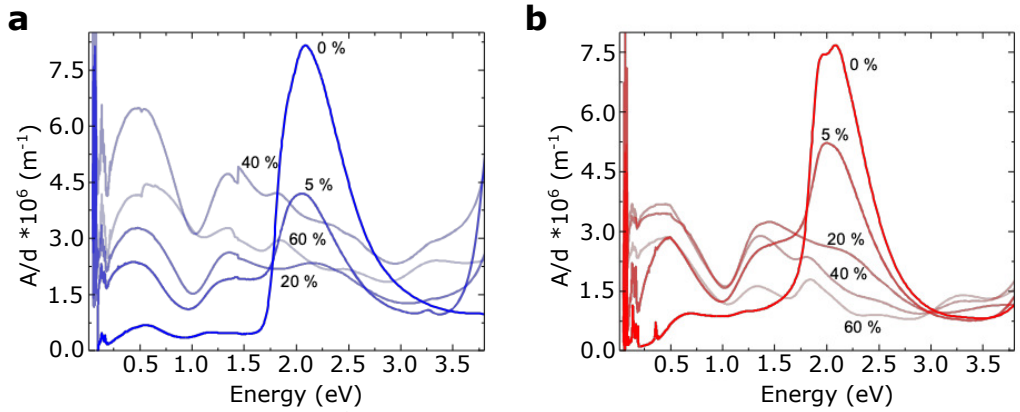

Figure 4.11: Results from analysis of the doped samples using UV-Vis-NIR absorption spectroscopy and FTIR on (a) p($g_3$2T-T) and (b) p($g_6$2T-T).

trations [32, 38], which is consistent with the conclusion that the dopant species are not blocked from charge transfer in the clusters. Interestingly, as dopant concentration is further increased to 40 and 60 mol%, there are deviations from the isosbestic point and another peak is appearing at 1.9 eV. The presence of a new peak indicates that a new electrical specie is formed in the material at high dopant concentrations. This new peak could correspond to polaron pairs or bipolarons. As discussed in section 2.1.3, a transition from polarons to polaron pairs or bipolarons should result in a negative effect on electrical conductivity. It should be noted that the appearance of the peak at 1.9 eV coincides with the decrease in electrical conductivity.

It can be observed in figure 4.11b that neat p($g_6$2T-T) exhibits similar spectral features as p($g_3$2T-T). However, as dopants are added there is less quenching of the HOMO-LUMO transition peak and less absorption from polaronic bands in p($g_6$2T-T) compared to p($g_3$2T-T). This indicates a lower charge transfer efficiency for the dopants in p($g_6$2T-T). The dopant ionisation efficiency was quantitatively evaluated by calculating the charge density from the polaron peaks in the absorption spectra. The calculated charge densities and resulting dopant ionisation efficiencies are shown in table 4.1.

These calculations confirm that, as the dopant concentration increases there is a significant decrease in dopant ionisation efficiency. Different electrical species have been discussed in section 2.1.3, and it should be noted that the calculations for charge density and ionisation efficiency only considers polarons. Thus, the formation of new electrical species at high dopant concentrations leads to underestima-

Table 4.1: Charge density and dopant ionisation efficiency of the doped samples. Values are calculated from optical absorption spectra (abs.) and tomography reconstructions (tomo.). Numbers marked * have added uncertainty due to the presence of additional electrical species. Note that the dopant can transfer two charges, thus yielding a maximum ionisation efficiency of 200 %. This double doping can be measured by the absorption spectroscopy, but is not accounted for in the tomography-based approximation.

	Dopant conc. [%]	**Char. dens. (abs.)** [$\mathbf{10^{26}}$ $\mathbf{m^{-3}}$]	**Ion. eff. (abs.)** [%]	**Char. dens. (tomo.)** [$\mathbf{10^{26}}$ $\mathbf{m^{-3}}$]	**Ion. eff. (tomo.)** [%]
p($g_3$2T-T)	5	0.21	118	0.14	78
	20	0.34	44	0.38	49
	40	0.66*	31*	0.39	19
	60	0.41*	8.6*	0.48	10
p($g_6$2T-T)	5	0.22	180	0.11	91
	20	0.28	35	0.23	29
	40	0.19*	8.7*	0.19	8.8
	60	0.016*	0.34*	0.42	8.7

tions of the values. Nonetheless, the ionisation efficiencies and charge densities are higher for p($g_3$2T-T) compared to p($g_6$2T-T), and higher charge density, n, leads to a higher conductivity, σ, according to $\sigma = q\mu n$. Thus, the measured charge density differences can explain the conductivity differences between the polymers.

Since the conductivity formula also includes charge mobility, μ, GIWAXS experiments were performed to get a better understanding of the polymer ordering in the thin-films. Experiments were performed on p($g_3$2T-T) and p($g_6$2T-T) doped with 20 mol% Mo(tfd-$COCF_3$)$_3$. The peaks in the resulting diffractograms which corresponds to polymer π-stacking were evaluated by calculating the coherence length and the paracrystallinity distortion parameter. These calculations yielded similar values for both polymer variants, indicating a similar degree of π-stacking and by extension no π-stacking induced differences in charge mobility μ between the samples. Thus, the differences in conductivity should mainly be attributed to differences in charge density.

The changes in electrical properties correlate with the changes in dopant distribution discussed in section 4.2. The samples containing larger and more elongated dopant clusters also exhibit lower ionisation efficiencies. Furthermore, the shorter

side-chain of p($g_3$2T-T) leads to both a finer dopant distribution and higher ionisation efficiencies. This can be explained by that the shorter side-chains may allow the dopants to get closer to the polymer backbone, resulting in a better access to host states that favour charge transfer. Since the dopants are not covalently bound to their positions, they can reorganise after charge transfer. At this point, ionised dopants should Coulombically repel other dopants with the same polarity, resulting in a lower tendency to form clusters. The presence of larger clusters in the tomography reconstructions indicates therefore a larger fraction of neutrally charged dopants which have not contributed with additional charges to the system. These neutral dopants do not increase conductivity, and additionally remain as inert features that potentially disrupt the polymer nanostructure at high dopant concentrations. Thus, the neutral dopants can have a negative impact on the conductivity.

The correlation between dopant ionisation efficiency and degree of clustering in the samples was further evaluated by estimating charge densities from the tomography reconstructions. By assuming that every cluster only contributes with one charge to the system, the charge densities could be estimated by using the average nearest-neighbour distance between clusters for each sample. These estimations of the charge densities, and the resulting dopant ionisation efficiencies, are displayed in table 4.1. The table shows that the estimated values follow the same trend as the calculated values from the optical absorption measurements, where the latter include double doping. The similarities in trend between the two types of measurements further support the correlation between clustering and ionisation efficiency.

The data presented in this section shows that the use of polythiophenes with short polar side-chains, such as p($g_3$2T-T), results in finer distribution of dopant molecules and more favourable electrical properties for the material. The results highlight the importance of structural characterisation, even at length-scales as small as the single nanometer for OSCs, since it provides information which is crucial for the understanding and optimisation of future organic electronic devices.

5 Conclusions and Outlook

In this thesis, electron microscopy was used to study the correlation between nanostructure and electrical properties of different organic semiconductors. The ability of the copolymer p[p($g_4$2T-T)-co-U] to form homogenous films was studied using HAADF-STEM. High-resolution imaging revealed similar structures for the copolymer and for neat p($g_4$2T-T), indicating that the urethane segments in the copolymer were successfully added without significant disruption of the p($g_4$2T-T) nanostructure. This non-disruptive addition enhanced mechanical robustness of the copolymer with only slight reductions of electrical properties from the inclusion of the urethane. This enabled the material to form free-standing films and increased its applicability as active layer in organic electronics.

The bilayer interface structure of the polymers BBL and p($g_4$2T-T) was studied by preparing cross-sections using the FIB-SEM lift-out scheme. Direct HAADF-STEM imaging of the detailed interface structure proved challenging due to the low contrast between the polymers. Instead, they could be distinguished using the spectroscopy technique EDXS-SI, which revealed a strong polymer separation with an interface that was only a few nanometres wide. This interface was of high importance for these polymers since it allowed the formation of a continuous charge transport layer with enhanced conductivity through the film. A BHJ of this material blend was created in order to maximise the interface area, resulting in a bulk material with a conductivity several orders of magnitude higher than that of the pure polymers.

The phase distribution in a BHJ of TQ1:$PC_{71}BM$ was also studied. Structural data regarding the fine-scale separation between the phases was obtained using BF-TEM and HAADF-STEM. This data was used to calibrate a KMC model, resulting in simulated J-V curves that more accurately described what have been experimentally observed for the system.

Furthermore, a method was developed for visualising the 3D spatial distribution of individual Mo(tfd-$COCF_3$)$_3$ molecular dopants in p($g_4$2T-T). By acquiring HAADF-STEM tilt series and performing electron tomography, the 3D dopant distribution in the material could be reconstructed with sub-nanometre resolu-

tion. Analysis of the reconstructions allowed the position of individual dopant species to be determined. The tomography reconstructions revealed both individual dopants and clusters a few nanometres in size. The method was repeated for polymers of different polar side-chain lengths, p($g_3$2T-T) and p($g_6$2T-T), and all polymers variants were analysed at different dopant concentrations. The results showed that the dopant clustering depended on dopant concentration, and that the clustering characteristics was affected by the side-chain length. Quantitative data was extracted from the reconstructed volumes, which revealed changes in cluster volumes, aspect ratios and distances to nearest neighbours for the different dopant concentrations. Despite that larger clusters were observed at higher dopant levels, the clusters remained sufficiently fine-dispersed to never fully block dopants from being adjacent to the surrounding polymer. Electrical measurements showed that the conductivity initially increased with increased dopant concentration and thereafter decreased as the clusters grew larger and increasingly elongated. All polymer variants exhibited these conductivity trends, but the absolute values were higher and maximum was reached at a lower dopant concentration for the short side-chains. A correlation could be observed between a saturation in the electrical conductivity and a significant increase in cluster size and aspect ratio. Additionally, optical absorption measurements revealed that new electrical species are formed at the same concentrations at which the degree of clustering increases. Dopant ionisation efficiencies were calculated from the optical absorption data, indicating that the dopant charge transfer efficiency decreases at higher concentrations but is overall higher for short polar side-chain polymers. The study suggested that short polar side-chains increase the dopants' access to the polymer backbone, resulting in higher ionisation efficiencies and higher conductivities. The higher fraction of ionised dopants leads to a lower tendency for dopant clustering, which is experimentally observed in the material.

The work in this thesis provides new insights regarding the functional nanostructure of organic semiconductor systems. Characterisation using electron microscopy imaging, spectroscopy and 3D reconstruction have yielded detailed information about fundamental mechanisms in these complex systems. A better fundamental understanding enables a better control of device-relevant properties and fabrication of optimised materials for future applications. However, numerous aspects regarding the functional nanostructure of organic semiconductor systems remain to be investigated, especially regarding doped semiconducting polymers. The details of dopant clustering can vary for different dopant and polymer combinations, and performing a detailed study of all relevant combinations is not practically feasible. A systematic approach to develop guidelines for dopant-polymer interactions would provide valuable information that benefits the development of doped

systems with high efficiencies. Another aspect which is important for the future success of organic electronics is long-term stability. Diffusion and drift of molecular dopants risk altering electrical properties across doped materials. Such changes over time would hamper the practical usefulness of organic electronics. The detailed drift of individual dopant species could potentially be studied using an *in situ* biasing setup in an electron microscope. By applying an electrical bias across a doped film and utilising a high Z-contrast dopant such as the one used in this thesis, the detailed drift and pathways of dopant molecules could potentially be imaged directly using HAADF-STEM. A thorough study of the dopant dynamics would provide new information regarding the motion of the molecules during device operation and how such movement can be controlled. Such a study is beyond the scope of this thesis, but could lead to novel strategies for an increased long-term stability of organic electronics.

Bibliography

[1] G. Persson. *Correlating nanostructure and electronic properties of organic semiconductors by electron microscopy*. Chalmers University of Technology, 2022.

[2] D. Todd. *The world electronics industry*. Routledge, 2018.

[3] S. Maldonado. The importance of new "sand-to-silicon" processes for the rapid future increase of photovoltaics. *ACS Energy Lett.*, **5**(11):3628–3632, 11 2020.

[4] P. R. Berger and M. Kim. Polymer solar cells: P3ht:pcbm and beyond. *J. Renew. Sustain. Energy*, **10**(1):013508, 2018.

[5] A. F. Paterson, S. Singh, K. J. Fallon, T. Hodsden, Y. Han, B. C. Schroeder, H. Bronstein, M. Heeney, I. McCulloch, and T. D. Anthopoulos. Recent progress in high-mobility organic transistors: A reality check. *Adv. Mater.*, **30**(36):1801079, 2018.

[6] D. Khodagholy, T. Doublet, P. Quilichini, M. Gurfinkel, P. Leleux, A. Ghestem, E. Ismailova, T. Hervé, S. Sanaur, C. Bernard, and G. G. Malliaras. In vivo recordings of brain activity using organic transistors. *Nat. Commun.*, **4**(1):1575, 2013.

[7] B. Lüssem, M. Riede, and K. Leo. Doping of organic semiconductors. *Phys. Status Solidi A*, **210**(1):9–43, 2013.

[8] I. E. Jacobs and A. J. Moulé. Controlling molecular doping in organic semiconductors. *Adv. Mater.*, **29**(42):1703063, 2017.

[9] D. T. Duong, C. Wang, E. Antono, M. F. Toney, and A. Salleo. The chemical and structural origin of efficient p-type doping in p3ht. *Org. Electron.*, **14**(5):1330–1336, 2013.

[10] J. E. Cochran, M. J. N. Junk, A. M. Glaudell, P. L. Miller, J. S. Cowart, M. F. Toney, C. J. Hawker, B. F. Chmelka, and M. L. Chabinyc. Molecular interactions and ordering in electrically doped polymers: Blends of pbttt and f4tcnq. *Macromolecules*, **47**(19):6836–6846, 2014.

[11] F. Liu, W. Zhao, J. R. Tumbleston, C. Wang, Y. Gu, D. Wang, A. L. Briseno, H. Ade, and T. P. Russell. Understanding the morphology of ptb7:pcbm blends in organic photovoltaics. *Adv. Energy Mater.*, 4(5):1301377, 2014.

[12] J. D. Roehling, D. Baran, J. Sit, T. Kassar, T. Ameri, T. Unruh, C. J. Brabec, and A. J. Moulé. Nanoscale morphology of ptb7 based organic photovoltaics as a function of fullerene size. *Sci. Rep.*, **6**(1):30915, 2016.

[13] B. Kuei, M. P. Aplan, J. H. Litofsky, and E. D. Gomez. New opportunities in transmission electron microscopy of polymers. *Mater. Sci. Eng. R Rep.*, **139**:100516, 2020.

[14] D. Lolla, J. Gorse, C. Kisielowski, J. Miao, P. L. Taylor, G. G. Chase, and D. H. Reneker. Polyvinylidene fluoride molecules in nanofibers, imaged at atomic scale by aberration corrected electron microscopy. *Nanoscale*, **8**:120–128, 2016.

[15] C. J. Takacs, N. D. Treat, S. Krämer, Z. Chen, A. Facchetti, M. L. Chabinyc, and A. J. Heeger. Remarkable order of a high-performance polymer. *Nano Lett*, **13**(6):2522–2527, 6 2013.

[16] C. Guo, F. I. Allen, Y. Lee, T. P. Le, C. Song, J. Ciston, A. M. Minor, and E. D. Gomez. Probing local electronic transitions in organic semiconductors through energy-loss spectrum imaging in the transmission electron microscope. *Adv. Funct. Mater.*, **25**(38):6071–6076, 2015.

[17] R. Ishikawa, E. Okunishi, H. Sawada, Y. Kondo, F. Hosokawa, and E. Abe. Direct imaging of hydrogen-atom columns in a crystal by annular bright-field electron microscopy. *Nat. Mater.*, **10**(4):278–281, 2011.

[18] S. D. Findlay, T. Saito, N. Shibata, Y. Sato, J. Matsuda, K. Asano, E. Akiba, T. Hirayama, and Y. Ikuhara. Direct imaging of hydrogen within a crystalline environment. *Appl. Phys. Express*, **3**(11):116603, 2010.

[19] D. B. Williams and C. B. Carter. *Transmission Electron Microscopy: A Textbook for Materials Science*. Springer Science+Business Media, 2 edition, 2009.

[20] R. F. Egerton. Radiation damage to organic and inorganic specimens in the tem. *Micron*, **119**:72–87, 2019.

[21] D. Natali. Fundamentals of organic electronic devices. In *Organic Flexible Electronics*, Woodhead Publishing Series in Electronic and Optical Materials, chapter 1, pages 1–25. Woodhead Publishing, 2021.

[22] R. M. Pankow and B. C. Thompson. The development of conjugated polymers as the cornerstone of organic electronics. *Polymer*, **207**:122874, 2020.

[23] H. Shirakawa, E. J. Louis, A. G. MacDiarmid, C. K. Chiang, and A. J. Heeger. Synthesis of electrically conducting organic polymers: halogen derivatives of polyacetylene, (ch). *J. Chem. Soc., Chem. Commun.*, pages 578–580, 1977.

[24] H. Bronstein, Christian B. N., B. C. Schroeder, and I. McCulloch. The role of chemical design in the performance of organic semiconductors. *Nat. Rev. Chem.*, **4**(2):66–77, 2020.

[25] C. Greco, A. Melnyk, K. Kremer, D. Andrienko, and K. C. Daoulas. Generic model for lamellar self-assembly in conjugated polymers: linking mesoscopic morphology and charge transport in p3ht. *Macromolecules*, **52**(3):968–981, 2019.

[26] C. Poelking, K. Daoulas, A. Troisi, and D. Andrienko. Morphology and charge transport in p3ht: A theorist's perspective. In *P3HT Revisited – From Molecular Scale to Solar Cell Devices*, pages 139–180. Springer Berlin Heidelberg, 2014.

[27] C. Poelking and D. Andrienko. Effect of polymorphism, regioregularity and paracrystallinity on charge transport in poly (3-hexylthiophene)[p3ht] nanofibers. *Macromolecules*, **46**(22):8941–8956, 2013.

[28] V. Coropceanu, J. Cornil, D. A. da Silva Filho, Y. Olivier, R. Silbey, and J.-L. Brédas. Charge transport in organic semiconductors. *Chem. Rev.*, **107**(4):926–952, 2007.

[29] H. Hase and I. Salzmann. Doping in organic semiconductors. In *Handbook of Organic Materials for Electronic and Photonic Devices*, Woodhead Publishing Series in Electronic and Optical Materials, pages 349–383. Woodhead Publishing, second edition, 2019.

[30] I. Salzmann, G. Heimel, M. Oehzelt, S. Winkler, and N. Koch. Molecular electrical doping of organic semiconductors: Fundamental mechanisms and emerging dopant design rules. *Acc. Chem. Res.*, **49**(3):370–378, 2016.

[31] I. Salzmann, G. Heimel, M. Oehzelt, S. Winkler, and N. Koch. Molecular electrical doping of organic semiconductors: fundamental mechanisms and emerging dopant design rules. *Acc. Chem. Res.*, **49**(3):370–378, 2016.

[32] H. Méndez, G. Heimel, S. Winkler, J. Frisch, A. Opitz, K. Sauer, B. Wegner, M. Oehzelt, C. Röthel, S. Duhm, D. Többens, N. Koch, and I. Salzmann.

Charge-transfer crystallites as molecular electrical dopants. *Nat. Commun.*, **6**(1):8560, 2015.

[33] I. Salzmann and G. Heimel. Toward a comprehensive understanding of molecular doping organic semiconductors (review). *J. Electron Spectros. Relat. Phenomena*, **204**:208–222, 2015.

[34] C. J. Boyle, M. Upadhyaya, P. Wang, L. A. Renna, M. Lu-Díaz, S. Pyo Jeong, N. Hight-Huf, L. Korugic-Karasz, M. D. Barnes, Z. Aksamija, and D. Venkataraman. Tuning charge transport dynamics via clustering of doping in organic semiconductor thin films. *Nat. Commun.*, **10**(1):2827, 2019.

[35] A. Fediai, A. Emering, F. Symalla, and W. Wenzel. Disorder-driven doping activation in organic semiconductors. *Phys. Chem. Chem. Phys.*, **22**:10256–10264, 2020.

[36] Norbert K. Charge carrier transport in organic semiconductors. *Synth. Met.*, **133**:649–657, 2003.

[37] S. Fratini, M. Nikolka, A. Salleo, G. Schweicher, and H. Sirringhaus. Charge transport in high-mobility conjugated polymers and molecular semiconductors. *Nat. Mater.*, **19**(5):491–502, 2020.

[38] J. L. Bredas and G. B. Street. Polarons, bipolarons, and solitons in conducting polymers. *Acc. Chem. Res.*, **18**(10):309–315, 1985.

[39] N. Lu, L. Li, D. Geng, and M. Liu. A review for polaron dependent charge transport in organic semiconductor. *Org. Electron.*, **61**:223–234, 2018.

[40] S. Giannini, A. Carof, M. Ellis, H. Yang, O. George Ziogos, S. Ghosh, and J. Blumberger. Quantum localization and delocalization of charge carriers in organic semiconducting crystals. *Nat. Commun.*, **10**(1):3843, 2019.

[41] E. C. Wu, C. Z. Salamat, O. L. Ruiz, T. Qu, A. Kim, S. H. Tolbert, and B. J. Schwartz. Counterion control and the spectral signatures of polarons, coupled polarons, and bipolarons in doped p3ht films. *Adv. Funct. Mater.*, **33**(19):2213652, 2023.

[42] A. Salleo, R. J. Kline, D. M. DeLongchamp, and M. L. Chabinyc. Microstructural characterization and charge transport in thin films of conjugated polymers. *Adv. Mater.*, **22**(34):3812–3838, 2010.

[43] R. Noriega, J. Rivnay, K. Vandewal, F. P. V. Koch, N. Stingelin, P. Smith, M. F. Toney, and A. Salleo. A general relationship between disorder, aggregation and charge transport in conjugated polymers. *Nat. Mater.*, **12**(11):1038–1044, 2013.

[44] R. A. Street, J. E. Northrup, and A. Salleo. Transport in polycrystalline polymer thin-film transistors. *Phys. Rev. B*, **71**(16):165202, 2005.

[45] J. Hynynen, E. Järsvall, R. Kroon, Y. Zhang, S. Barlow, S. R. Marder, M. Kemerink, A. Lund, and C. Müller. Enhanced thermoelectric power factor of tensile drawn poly(3-hexylthiophene). *ACS Macro Lett.*, **8**(1):70–76, 2019.

[46] L. Biniek, N. Leclerc, T. Heiser, R. Bechara, and M. Brinkmann. Large scale alignment and charge transport anisotropy of pbttt films oriented by high temperature rubbing. *Macromolecules*, **46**(10):4014–4023, 2013.

[47] A. Salleo. Charge transport in polymeric transistors. *Mater. Today*, **10**(3):38–45, 2007.

[48] C. Cendra, L. Balhorn, W. Zhang, K. O'Hara, K. Bruening, C. J. Tassone, H.-G. Steinrück, M. Liang, M. F. Toney, I. McCulloch, M. L. Chabinyc, A Salleo, and C. J. Takacs. Unraveling the unconventional order of a high-mobility indacenodithiophene–benzothiadiazole copolymer. *ACS Macro Lett.*, **10**(10):1306–1314, 2021.

[49] P. Scherrer. Bestimmung der grösse und inneren struktur von kolloidteilchen mittels röntgenstrahlen. *Nach. Ges. Wiss. Gottingen*, **2**:8–100, 1918.

[50] A. M. Hindeleh and R. Hosemann. Paracrystals representing the physical state of matter. *J. Phys. C: Solid State Phys.*, **21**(23):4155, 1988.

[51] J. E. Cochran, M. J. N. Junk, A. M. Glaudell, P. L. Miller, J. S. Cowart, M. F. Toney, C. J. Hawker, B. F. Chmelka, and M. L. Chabinyc. Molecular interactions and ordering in electrically doped polymers: Blends of pbttt and f4tcnq. *Macromolecules*, **47**(19):6836–6846, 2014.

[52] H. Kleemann, C. Schuenemann, A. A. Zakhidov, M. Riede, B. Lüssem, and K. Leo. Structural phase transition in pentacene caused by molecular doping and its effect on charge carrier mobility. *Org. Electron.*, **13**(1):58–65, 2012.

[53] F. Deschler, D. Riedel, A. Deák, B. Ecker, E. von Hauff, and E. Da Como. Imaging of morphological changes and phase segregation in doped polymeric semiconductors. *Synth. Met.*, **199**:381–387, 2015.

[54] J. Euvrard, A. Revaux, P.-A. Bayle, M. Bardet, D. Vuillaume, and A. Kahn. The formation of polymer-dopant aggregates as a possible origin of limited doping efficiency at high dopant concentration. *Org. Electron.*, **53**:135–140, 2018.

[55] D. Donhauser, M. Pfannmöller, L. Dieterle, K. Schultheiß, R. R. Schröder,

W. Kowalsky, and M. Kröger. Observation of filamentous nanostructures in organic-inorganic composite thin films deposited by co-evaporation. *Adv. Funct. Mater.*, **23**(17):2130–2136, 2013.

[56] I. E. Jacobs, E. W. Aasen, J. L. Oliveira, T. N. Fonseca, J. D. Roehling, J. Li, G. Zhang, M. P. Augustine, M. Mascal, and A. J. Moulé. Comparison of solution-mixed and sequentially processed p3ht: F4tcnq films: effect of doping-induced aggregation on film morphology. *J. Mater. Chem. C*, **4**(16):3454–3466, 2016.

[57] J. Hynynen, D. Kiefer, L. Yu, R. Kroon, R. Munir, A. Amassian, M. Kemerink, and C. Müller. Enhanced electrical conductivity of molecularly p-doped poly(3-hexylthiophene) through understanding the correlation with solid-state order. *Macromolecules*, **50**(20):8140–8148, 2017.

[58] J. Li, C. Koshnick, S. O. Diallo, S. Ackling, D. M. Huang, I. E. Jacobs, T. F. Harrelson, K. Hong, G. Zhang, J. Beckett, M. Mascal, and A. J. Moulé. Quantitative measurements of the temperature-dependent microscopic and macroscopic dynamics of a molecular dopant in a conjugated polymer. *Macromolecules*, **50**(14):5476–5489, 2017.

[59] S. A. Paniagua, J. Baltazar, H. Sojoudi, S. K. Mohapatra, S. Zhang, C. L. Henderson, S. Graham, S. Barlow, and S. R. Marder. Production of heavily n- and p-doped cvd graphene with solution-processed redox-active metal–organic species. *Mater. Horiz.*, **1**:111–115, 2014.

[60] S. K. Mohapatra, Y. Zhang, B. Sandhu, M. S. Fonari, T. V. Timofeeva, S. R. Marder, and S. Barlow. Synthesis, characterization, and crystal structures of molybdenum complexes of unsymmetrical electron-poor dithiolene ligands. *Polyhedron*, **116**:88–95, 2016.

[61] N. C. Cates, R. Gysel, Z. Beiley, C. E. Miller, M. F. Toney, M. Heeney, I. McCulloch, and M. D. McGehee. Tuning the properties of polymer bulk heterojunction solar cells by adjusting fullerene size to control intercalation. *Nano Lett.*, **9**(12):4153–4157, 2009.

[62] P. Reiser, L. Müller, V. Sivanesan, R. Lovrincic, S. Barlow, S. R. Marder, A. Pucci, W. Jaegermann, E. Mankel, and S. Beck. Dopant diffusion in sequentially doped poly(3-hexylthiophene) studied by infrared and photoelectron spectroscopy. *J. Phys. Chem. C*, **122**(26):14518–14527, 2018.

[63] L. Müller, S.-Y. Rhim, V. Sivanesan, D. Wang, S. Hietzschold, P. Reiser, E. Mankel, S. Beck, S. Barlow, S. R. Marder, A. Pucci, W. Kowalsky, and

R. Lovrincic. Electric-field-controlled dopant distribution in organic semiconductors. *Adv. Mater.*, **29**(30):1701466, 2017.

[64] D. Kiefer, R. Kroon, A. I. Hofmann, H. Sun, X. Liu, A. Giovannitti, D. Stegerer, A. Cano, J. Hynynen, L. Yu, Y. Zhang, D. Nai, T. F. Harrelson, M. Sommer, A. J. Moulé, M. Kemerink, S. R. Marder, I. McCulloch, M. Fahlman, S. Fabiano, and C. Müller. Double doping of conjugated polymers with monomer molecular dopants. *Nat. Mater.*, **18**(2):149–155, 2019.

[65] V. Vijayakumar, E. Zaborova, L. Biniek, H. Zeng, L. Herrmann, A. Carvalho, O. Boyron, N. Leclerc, and M. Brinkmann. Effect of alkyl side chain length on doping kinetics, thermopower, and charge transport properties in highly oriented f4tcnq-doped pbttt films. *ACS Appl. Mater. Interfaces*, **11**(5):4942–4953, 2019.

[66] A. Hamidi-Sakr, L. Biniek, J.-L. Bantignies, D. Maurin, L. Herrmann, N. Leclerc, P. Lévêque, V. Vijayakumar, N. Zimmermann, and M. Brinkmann. A versatile method to fabricate highly in-plane aligned conducting polymer films with anisotropic charge transport and thermoelectric properties: The key role of alkyl side chain layers on the doping mechanism. *Adv. Funct. Mater.*, **27**(25):1700173, 2017.

[67] R. Kroon, D. Kiefer, D. Stegerer, L. Yu, M. Sommer, and C. Müller. Polar side chains enhance processability, electrical conductivity, and thermal stability of a molecularly p-doped polythiophene. *Adv. Mater.*, **29**(24):1700930, 2017.

[68] J. Liu, L. Qiu, G. Portale, S. Torabi, M. C. A. Stuart, X. Qiu, M. Koopmans, R. C. Chiechi, J. C. Hummelen, and L. J. Anton Koster. Side-chain effects on n-type organic thermoelectrics: A case study of fullerene derivatives. *Nano Energy*, **52**:183–191, 2018.

[69] M. Craighero, J. Guo, S. Zokaei, S. Griggs, J. Tian, J. Asatryan, J. Kimpel, R. Kroon, K. Xu, J. S. Reparaz, J. Martín, I. McCulloch, M. Campoy-Quiles, and C. Müller. Impact of oligoether side-chain length on the thermoelectric properties of a polar polythiophene. *ACS Appl. Electron. Mater.*, 2023.

[70] W. Tress. *Organic Solar Cells*, chapter 1. Springer International Publishing, 2014.

[71] National Renewable Energy Laboratory. Best research-cell efficiency chart, Jan 2024.

[72] A. Feltrin and A. Freundlich. Material considerations for terawatt level deployment of photovoltaics. *Renew. Energy*, **33**(2):180–185, 2008.

[73] G. J. Hedley, A. Ruseckas, and I. D. W. Samuel. Light harvesting for organic photovoltaics. *Chem. Rev.*, **117**(2):796–837, 2017.

[74] L. Lu, T. Zheng, Q. Wu, A. M. Schneider, D. Zhao, and L. Yu. Recent advances in bulk heterojunction polymer solar cells. *Chem. Rev.*, **115**(23):12666–12731, 2015.

[75] W. R. Mateker and M. D. McGehee. Progress in understanding degradation mechanisms and improving stability in organic photovoltaics. *Adv. Mater.*, **29**(10):1603940, 2017.

[76] M. Pfannmoller, H. Flugge, G. Benner, I. Wacker, C. Sommer, M. Hanselmann, S. Schmale, H. Schmidt, F. A. Hamprecht, T. Rabe, W. Kowlasky, and R. R. Schröder. Visualizing a homogeneous blend in bulk heterojunction polymer solar cells by analytical electron microscopy. *Nano Lett.*, **11**(8):3099–3107, 2011.

[77] P. Westacott, J. R Tumbleston, S. Shoaee, S. Fearn, J. H. Bannock, J. B. Gilchrist, S. Heutz, J. DeMello, M. Heeney, H. Ade, J. Durrant, D. S. McPhail, and N. Stingelin. On the role of intermixed phases in organic photovoltaic blends. *Energy Environ. Sci.*, **6**(9):2756–2764, 2013.

[78] S. Marina, N. P. Kaufmann, A. Karki, E. Gutiérrez-Meza, E. Gutiérrez-Fernández, J. Vollbrecht, E. Solano, B. Walker, J. H. Bannock, J. de Mello, C. Silva, T.-Q. Nguyen, D. Cangialosi, N. Stingelin, and J. Martín. The importance of quantifying the composition of the amorphous intermixed phase in organic solar cells. *Adv. Mater.*, **32**(47):2005241, 2020.

[79] D. Baran, R. S. Ashraf, D. A. Hanifi, M. Abdelsamie, N. Gasparini, J. A. Röhr, S. Holliday, A. Wadsworth, S. Lockett, M. Neophytou, C. J. M. Emmott, J. Nelson, C. J. Brabec, A. Amassian, A. Salleo, T. Kirchartz, J. R. Durrant, and I. McCulloch. Reducing the efficiency–stability–cost gap of organic photovoltaics with highly efficient and stable small molecule acceptor ternary solar cells. *Nat. Mater.*, **16**(3):363–369, 2017.

[80] M. Jørgensen, K. Norrman, and F. C. Krebs. Stability/degradation of polymer solar cells. *Sol. Energy Mater. Sol. Cells*, **92**(7):686–714, 2008.

[81] S. A. Gevorgyan, M. V. Madsen, B. Roth, M. Corazza, M. Hösel, R. R. Søndergaard, M. Jörgensen, and F. C. Krebs. Lifetime of organic photovoltaics: Status and predictions. *Adv. Energy Mater.*, **6**(2):1501208, 2016.

[82] Y. Wei, Z. Chen, G. Lu, N. Yu, C. Li, J. Gao, X. Gu, X. Hao, G. Lu, Z. Tang, J. Zhang, Z. Wei, X. Zhang, and H. Huang. Binary organic solar

cells breaking 19% via manipulating the vertical component distribution. *Adv. Mater.*, **34**(33):2204718, 2022.

[83] G. Han, Y. Yi, and Z. Shuai. From molecular packing structures to electronic processes: Theoretical simulations for organic solar cells. *Adv. Energy Mater.*, **8**(28):1702743, 2018.

[84] X. Zhang and L.-D. Zhao. Thermoelectric materials: Energy conversion between heat and electricity. *J. Materiomics*, **1**(2):92–105, 2015.

[85] B. Wang and A. Facchetti. Mechanically flexible conductors for stretchable and wearable e-skin and e-textile devices. *Adv. Mater.*, **31**(28):1901408, 2019.

[86] Daniel C. Thermoelectric generators: A review of applications. *Energy Convers. Manag.*, **140**:167–181, 2017.

[87] B. Russ, A. Glaudell, J. J. Urban, M. L. Chabinyc, and R. A. Segalman. Organic thermoelectric materials for energy harvesting and temperature control. *Nat. Rev. Mater.*, **1**(10):16050, 2016.

[88] G. Chen, W. Xu, and D. Zhu. Recent advances in organic polymer thermoelectric composites. *J. Mater. Chem. C*, **5**:4350–4360, 2017.

[89] R. Kroon, D. A. Mengistie, D. Kiefer, J. Hynynen, J. D. Ryan, L. Yu, and C. Müller. Thermoelectric plastics: from design to synthesis, processing and structure–property relationships. *Chem. Soc. Rev.*, **45**:6147–6164, 2016.

[90] S. N. Patel, A. M. Glaudell, K. A. Peterson, E. M. Thomas, K. A. O'Hara, E. Lim, and M. L. Chabinyc. Morphology controls the thermoelectric power factor of a doped semiconducting polymer. *Sci. Adv*, **3**(6), 2017.

[91] S. Guchait, Y. Zhong, and M. Brinkmann. High-temperature rubbing: An effective method to fabricate large-scale aligned semiconducting and conducting polymer films for applications in organic electronics. *Macromolecules*, **56**(17):6733–6757, 2023.

[92] T. Someya, Z. Bao, and G. G. Malliaras. The rise of plastic bioelectronics. *Nature*, **540**(7633):379–385, 2016.

[93] H. Yao, Z. Fan, H. Cheng, X. Guan, C. Wang, K. Sun, and J. Ouyang. Recent development of thermoelectric polymers and composites. *Macromol. Rapid Commun.*, **39**(6):1700727, 2018.

[94] M. R. Andersson, O. Thomas, W. Mammo, M. Svensson, M. Theander, and O. Inganäs. Substituted polythiophenes designed for optoelectronic devices and conductors. *J. Mater. Chem.*, **9**:1933–1940, 1999.

[95] A. Fediai, A. Emering, F. Symalla, and W. Wenzel. Disorder-driven doping activation in organic semiconductors. *Phys. Chem. Chem. Phys.*, **22**:10256–10264, 2020.

[96] A. Bafekry, M. M. Fadlallah, C. Nguyen, and D. Gogova. Vertical two-dimensional layered conjugated porous organic network structures of polybenzimidazobenzophenanthroline (bbl): A first-principles study. *Appl. Phys. Lett.*, **117**(23):233101, 2020.

[97] J. Lee, A. J. Kalin, T. Yuan, M. Al-Hashimi, and L. Fang. Fully conjugated ladder polymers. *Chem. Sci.*, **8**:2503–2521, 2017.

[98] C. Lindqvist, A. Sanz-Velasco, E. Wang, O. Bäcke, S. Gustafsson, E. Olsson, M. R. Andersson, and C. Müller. Nucleation-limited fullerene crystallisation in a polymer–fullerene bulk-heterojunction blend. *J. Mater. Chem. A*, **1**:7174–7180, 2013.

[99] L. Hou, E. Wang, J. Bergqvist, B. V. Andersson, Z. Wang, C. Müller, M. Campoy-Quiles, M. R. Andersson, F. Zhang, and O. Inganäs. Lateral phase separation gradients in spin-coated thin films of high-performance polymer:fullerene photovoltaic blends. *Adv. Funct. Mater.*, **21**(16):3169–3175, 2011.

[100] D. J. Lipomi and Z. Bao. Stretchable and ultraflexible organic electronics. *MRS Bull.*, **42**(2):93–97, 2017.

[101] S. K. Gupta, P. Jha, A. Singh, M. M. Chehimi, and D. K. Aswal. Flexible organic semiconductor thin films. *J. Mater. Chem. C*, **3**:8468–8479, 2015.

[102] G. H. Michler. *Electron Microscopy of Polymers*. Springer Laboratory. Springer Berlin Heidelberg, 2008.

[103] J. I. Goldstein, D. E. Newbury, J. R. Michael, N. W. M. Ritchie, J. H. J. Scott, and D. C. Joy. *Scanning electron microscopy and X-ray microanalysis*. Springer New York, 4 edition, 2017.

[104] L. Reimer. *Transmission Electron Microscopy: Physics of Image Formation and Microanalysis*, volume **36**. Springer Berlin Heidelberg, 2013.

[105] S. J. Pennycook and P. D. Nellist. *Scanning Transmission Electron Microscopy: Imaging and Analysis*. Springer New York, 2011.

[106] R. F Egerton. *Electron energy-loss spectroscopy in the electron microscope*. Springer Science & Business Media, 3 edition, 2011.

[107] P. A. Midgley and R. E. Dunin-Borkowski. Electron tomography and holography in materials science. *Nat. Mater.*, **8**(4):271–280, 2009.

[108] R. A. Crowther, D. J. DeRosier, and A. Klug. The reconstruction of a three-dimensional structure from projections and its application to electron microscopy. *Proc. R. Soc. London A. Math. Phys. Sci.*, **317**(1530):319–340, 1970.

[109] A. Bartesaghi, P. Sprechmann, J. Liu, G. Randall, G. Sapiro, and S. Subramaniam. Classification and 3d averaging with missing wedge correction in biological electron tomography. *J. Struct. Biol.*, **162**(3):436–450, 2008.

[110] L. Paavolainen, E. Acar, U. Tuna, S. Peltonen, T. Moriya, P. Soonsawad, V. Marjomäki, R. H. Cheng, and U. Ruotsalainen. Compensation of missing wedge effects with sequential statistical reconstruction in electron tomography. *PLOS One*, **9**(10):1–14, 2014.

[111] P. Ercius, O. Alaidi, M. J. Rames, and G. Ren. Electron tomography: A three-dimensional analytic tool for hard and soft materials research. *Adv. Mater.*, **27**(38):5638–5663, 2015.

[112] D. Shindo and T. Oikawa. *Energy Dispersive X-ray Spectroscopy*, pages 81–102. Springer Japan, Tokyo, 2002.

[113] G. Cliff and G. W. Lorimer. The quantitative analysis of thin specimens. *J. Microsc.*, **103**(2):203–207, 1975.

[114] M. Watanabe and D. B. Williams. The quantitative analysis of thin specimens: a review of progress from the cliff-lorimer to the new ζ-factor methods. *J. Microsc.*, **221**(2):89–109, 2006.

[115] A. J. D'Alfonso, B. Freitag, D. Klenov, and L. J. Allen. Atomic-resolution chemical mapping using energy-dispersive x-ray spectroscopy. *Phys. Rev. B*, **81**:100101, 2010.

[116] Z. Chen, M. Weyland, X. Sang, W. Xu, J. H. Dycus, J. M. LeBeau, A. J. D'Alfonso, L. J. Allen, and S. D. Findlay. Quantitative atomic resolution elemental mapping via absolute-scale energy dispersive x-ray spectroscopy. *Ultramicroscopy*, **168**:7–16, 2016.

[117] R. F. Egerton, R. McLeod, F. Wang, and M. Malac. Basic questions related to electron-induced sputtering in the tem. *Ultramicroscopy*, **110**(8):991–997, 2010.

[118] Q. Chen, C. Dwyer, G. Sheng, C. Zhu, X. Li, C. Zheng, and Y. Zhu.

Imaging beam-sensitive materials by electron microscopy. *Adv. Mater.*, **32**(16):1907619, 2020.

[119] Y. Lee, S. Lee, J.-Y. Yoon, J. Cheon, H. Y. Jeong, and K. Kim. Fabrication and imaging of monolayer phosphorene with preferred edge configurations via graphene-assisted layer-by-layer thinning. *Nano Lett.*, **20**(1):559–566, 1 2020.

[120] B. Kuei and E. D. Gomez. Elucidating mechanisms for electron beam damage in conjugated polymers. *Microsc. and Microanal.*, **24**(S1):1988–1989, 2018.

[121] O. Bäcke, Camilla L., A. Diaz de Zerio Mendaza, S. Gustafsson, E. Wang, M. R. Andersson, C. Müller, and E. Olsson. Mapping fullerene crystallization in a photovoltaic blend: an electron tomography study. *Nanoscale*, **7**:8451–8456, 2015.

[122] S. T. Salammal, E. Mikayelyan, S. Grigorian, U. Pietsch, N. Koenen, U. Scherf, N. Kayunkid, and M. Brinkmann. Impact of thermal annealing on the semicrystalline nanomorphology of spin-coated thin films of regioregular poly(3-alkylthiophene)s as observed by high-resolution transmission electron microscopy and grazing incidence x-ray diffraction. *Macromolecules*, **45**(13):5575–5585, 7 2012.

[123] J. Ayache, L. Beaunier, J. Boumendil, G. Ehret, and D. Laub. *Sample Preparation Handbook for Transmission Electron Microscopy: Techniques*. Sample preparation handbook for transmission electron microscopy / Jeanne Ayache; Luc Beaunier; Jacqueline Boumendil; Gabrielle Ehret; Danièle Laub. Foreword by Ron Anderson. Springer New York, 2010.

[124] M. Corazza, S. B. Simonsen, H. Gnaegi, K. T.S. Thydén, F. C. Krebs, and S. A. Gevorgyan. Comparison of ultramicrotomy and focused-ion-beam for the preparation of tem and stem cross section of organic solar cells. *Appl. Surf. Sci.*, **389**:462–468, 2016.

[125] Z. Ma, H. Geng, D. Wang, and Z. Shuai. Influence of alkyl side-chain length on the carrier mobility in organic semiconductors: herringbone vs. pi–pi stacking. *J. Mater. Chem. C*, **4**:4546–4555, 2016.

[126] H. Abdalla, G. Zuo, and M. Kemerink. Range and energetics of charge hopping in organic semiconductors. *Phys. Rev. B*, **96**:241202, 2017.